Functional and structural analyses of the terminal organelle of *Mycoplasma genitalium*

Luis González González

2015

Doctoral dissertation submitted to fulfil the requirements to obtain the Doctor of Phylosophy Degree in Bioquímica, Biologia Molecular i Biomedicina at Universitat Autònoma de Barcelona

This work has been performed at the Institut de Biotecnologia i Biomedicina in the Departament de Bioquimica i Biologia molecular under the supervision of Dr. Jaume Piñol Ribas and Dr. Enrique Querol Murillo

7. Chapter IV: Structural characterization of macromolecular complexes of *Mycoplasma genitalium* by electron microscopy[5]

7.1 Introduction

7.1.1 Cryo-electron microscopy and cryo-electron tomography

Electron microscopy takes advantage of the small wavelength of accelerated electrons to gain high-resolution imaging information of the sample analysed. Electrons need to be focused and travel from the source till the detector in high vacuum conditions to avoid scattering in collision with the subatomic components of air particles. Since the first electron microscope was built in 1931 by Ruska and Knoll, a huge panoply of them have been developed and further improved. These microscopes allow to analyse biological samples with an incredible detail level. In fact, using single-particle Cryo-EM, structure determination at resolutions below 0.4 nm has been achieved in the structure determination of different proteins or protein complexes (Cheng, 2015). This means that electron microscopy is currently providing structural details at near-atomic level. The most relevant types of electron microscopes aimed for biology include:

- Transmission electron microscopy (TEM): a high voltage generator produces high energy electrons capable of penetrate and go through the sample. A detector collects the electron beam after passing through the sample generating an image. Nowadays, the most common detectors are phosphor/fibre optics-coupled CCD/CMOS detector or the recently developed electron counting direct detection cameras (Gatan K2 or FEI Falcon). In the first type, a scintillator (*e.g.* phosphor screen) emit photons after electron impact and the CCD/CMOS camera collects those photons and creates and image of the specimen. The second type of camera is capable of directly counting the number of electrons that impact on its surface. The advantages of the second camera type are numerous, but the most important is the higher—up to 5x—DQE (detective quantum efficiency). DQE measures the ratio between the output signal-to-noise

[5] Cryo-electron tomography studies were carried out at BMLS (Bunchmann Institute for Molecular Life Sciences, Frankfurt, Germany) in collaboration with Achilleas S. Frangakis group. Subtomogram averaging was carried out by Zhou Yu.
Single particle negative staining analyses were fully performed at CNB (Centro Nacional de Biotecnologia, Madrid, Spain) in collaboration with Jaime Martín Benito and José Maria Valpuesta who performed automated image acquisition, particle picking and single particle averaging.
Particle purification for single particle negative staining was done in collaboration with Mercè Ratera and Ignasi Fita (CSIC, Barcelona, Spain).

ratio (SNR) in comparison with the input SNR meaning that, under the same imaging conditions, the signal is up to 5 times better in direct detection cameras (Grigorieff, 2013) and therefore it results in better reconstructions(Bammes et al., 2012). Since penetration through the sample is required for imaging, only thin biological specimens can be observed by TEM.

- Scanning electron microscopy (SEM): in this electron microscopy modality electron penetration in the sample is not required. A tightly focused electron beam scans line by line the sample surface. Electron collision on the sample causes the generation of secondary electrons. Both scattered electrons and secondary electrons are detected and software processed to create the final image. Thicker and larger specimens than in TEM can be analysed. In chapter I, II and III examples of SEM of mycoplasma cells attached to a glass surface have been presented.
- Focused ion beam (FIB): although it does not belong to the 'electron microscopy family' since it uses ions for imaging, its combination with SEM raised many new applications. FIB uses ions to mill the surface of the sample being analysed, allowing the penetration in the subject of study—although destroying the sample in the process—and obtaining high resolution SEM imaging immediately after the milling. This process can be easily automated for obtaining high resolution three dimensional SEM data of large specimens.

Conventional electron microscopy require biostructures to be protected from the high vacuum conditions by fixatives. In addition, these samples normally require to be stained by metal compounds to enhance the poor contrast of biological specimens. Methodologies for sample preparation include direct negative staining, thin-sectioning, cryo-fixation, freeze-fracturing and freeze-substitution. Some of these methodologies are fully compatible with immunolabeling, which allows to determine the subcellular location of the compounds interest under the electron beam. These processes have been proven to cause artefacts in biological structures. For this reason cryo-electron microscopy (cryo-EM) was developed. Cryo-EM allows biological specimens to be observed in a fully hydrated state, and does not require contrast-enhancing metal stains or chemical fixatives. Cryo-EM is performed in modified TEM microscopes. When performing cryo-EM in those microscopes, the sample and its holder are at liquid nitrogen temperature—196°C—which prevents evaporation of the water in the hydrated sample in high vacuum conditions. However, biological samples cannot be directly cooled to liquid nitrogen temperature due to water crystallization and expansion, which normally destroys or perturbs biological structures. Luckily, some liquid cryogens, such as ethane or propane, have the capacity to cool at rates higher than 13 kK/s.

This extremely quick freezing vitrifies the water in the sample, avoiding the formation of ice crystals, thus preserving the nearest possible frozen state of a biological specimen. Given the low sample thickness required for TEM microscopy, heat transfer in the sample is normally homogeneous when the sample is plunged in the cryogen (Dubochet et al., 1982). Plunge freezing is the gold standard for quick sample preparation for Cryo-EM since it only needs a cooled cryogen and a device to rapidly submerge the sample in this cryogen. Sample can be grown or applied on the observation surface just prior the plunge, but it is critical to blot it enough for obtaining a thin ice layer—as low as few nanometers—but not too much to avoid dehydrating the sample. Once the sample is vitrified it can be directly change to liquid nitrogen and stored or visualized by cryo-EM.

High pressure freezing has also been developed as a methodology to preserve biological structures upon sample cooling to liquid nitrogen temperatures. This approach is based in applying cryoprotectants and high pressures and while slowly freezing the sample, avoiding the nucleation and growth of ice crystals, this process is usually more tedious than plunge freezing, and for TEM it usually needs posterior cryo-sectioning.

Previous to 2013 the most common methodologies to obtain subnanometer resolution structures of proteins were NMR and X-ray crystallography. NMR is limited to relative small polypeptides. X-ray crystallography has proven to be widely useful—and the most successful approach—for both small and large proteinaceous entities (Jones, 2014, Shi, 2014), but it relies on the finding of crystallization conditions. Finding those conditions is often a stochastic process, being a huge bottleneck in the process to obtain the crystallographic structure of most proteins. Both methodologies also required high sample concentrations—usually in the order of tens of milligrams or even higher. Single particle cryo-EM is based in the computational combination of images from thousands of individual molecules in the same conformations (Frank et al., 1978, Frank, 1996)). This computational averaging relies in the improvement of resolution and SNR after averaging the projection images of biological particles. This projections are cut-out, aligned and then averaged. If the proper averaging protocols are employed, this will result in a 3D structure. Normally these averaging protocols rely on an iterative process of alignment to a reference (applying rotations in all angles necessary) and averaging. The process is normally repeated until the cross-correlation scores does not longer support an improvement of the 3D structure. Classification procedures are normally used for the differentiation of different conformations of the subject of study, or to discard aberrant ones. The first step of single particle EM relies in the isolation and purification of the protein(s) of interest with the highest purity and homogeneity possible. Then the sample is applied to the surface of examination in a

concentration that allows a high density of individual and isolated particles per field of visualization. Then the sample can be metal stained, often negative staining, or directly plunge frozen. If the sample is homogeneous enough automatic image acquisition and particle selection is performed to be later computationally analysed in order to obtain an average structure. This methodology was initially employed in negative staining single particle electron microscopy, obtaining intermediate resolution structures (Frank, 1996). Later on, it was applied in cryo-EM obtained data also with success (Typke et al., 2004). Numerous microscopes, hardware and software improvements lead to the first atomic level *de novo* structure determination in 2010 (Zhang et al., 2010). This method is currently being applied to obtain a growing number of cryo-EM structures of many proteins of interest and it is thought that it can equal or even surpass X-ray crystallography in terms of throughput over the coming years.

It is important to note that two major factors in cryo-EM limit resolution and experiment viability: the dose applied to the sample and the defocus used for image acquisition. First of all, biological samples suffer from radiation damage, so the higher the resolution wants to be achieved, the lower the dose should be applied to the sample. At lowers doses though, the SNR ratio is worse. The second factor that is also critical—the defocus applied to the sample—is in inverse correlation with the maximum resolution that can be achieved. Lowering the dose and the defocus at minimum is not possible, since contrast is positively correlated to the amount of dose and defocus applied to the sample. It has been demonstrated that working at very low contrast levels lead to debateable results (Mao et al., 2013, Henderson, 2013). Therefore for each sample—depending on the size, thickness, desired resolution, etc.—the proper amount of dose and defocus has to be found to obtain a good contrast and resolution while not damaging the sample. The rapid improvements in hardware and software (zero-loss filtering, better SNR, dose fractionation, etc.) greatly help to circumvent this problem.

7.1.2 Cryo-electron tomography

When analysing unprocessed thicker specimens—complexes analysed by single particle EM are rarely bigger than tens of nanometers—tomography is usually the methodology of choice. Complexes within cells or other structures are impossible to average by single particle cryo-EM since the elements below and above the object of interest superimpose in the image. Tomography is not only a cryo-EM method since it is normally used for plastic-embedded samples, but it has been widely employed in combination with cryo-EM for the analysis of multiple macromolecular complexes within the intact cells in its nearest-native

state achieved to date (Milne and Subramaniam, 2009, Tocheva et al., 2010, Li and Jensen, 2009).

Cryo-electron tomography (CET), relies in the acquisition of a series of images while rotating the sample perpendicular to the optical axis of the electron path. Computational combination of those serial images allows to obtain a volumetric reconstruction of the specimen. Different considerations should be taken into account when working with CET. One of the most important is that the number of inelastic collisions increase while rotating given that the effective ice thickness increases gradually when getting closer to extreme angles. It is impossible to rotate a specimen 180 degrees simply because the sample holder would obstruct the electrons to reach the object of study. For this reason, some of the views of the specimen are missing, creating a gap of information known as the 'missing-wedge'. Given that cells or other specimens studied are pleomorphic, entire volumetric reconstructions cannot be averaged, so the only way to completely avoid the 'missing-wedge problem" is cropping and averaging selected particles within the reconstruction. Although dual axis tomography has also been developed to overcome this handicap, its use has been not stablished as a standard for tomography.

CET is normally employed in heterogeneous virus particles, organelles or parts of the cells, but cells of some species, as those belonging to the mycoplasma genus, are small enough to be entirely analysed by cryo-EM.

For tomography of whole cells, they are directly applied to the examination surface or grown over it just prior to plunge freezing them, and then directly analysed by cryo-TEM. Since tomography later requires the alignment of the images obtained, fiducial markers on to the sample should be added previously to the plunge freezing. Fiducial markers are normally gold particles, coupled to a hydrophilic partner to enhance solubility and homodispersion, such as protein A.

While in single particle 2D projections of biological items can be computationally processed for structure determination, in CET 3D fragments of the volume generated can be computationally averaged to obtain also a 3D structure. This process is called subtomogram averaging. The main two differences between subtomogram averaging and single particle reconstruction is that the particles need to be selected in a 3D volume, and usually the computational requirements are higher since each particle is itself three-dimensional data. Interestingly, with subtomogram averaging the data obtained is not only the structure of the molecule of study, but also its spatial distribution and the number of copies in the sample, which is a valuable information as well. Subtomogran averaging has been applied for

obtaining the structures of numerous complexes and large proteins(Briggs, 2013) and, more recently, even the determination of structures at subnanometer resolution has been achieved(Schur et al., 2013, Schur et al., 2015). Hybrid image processing methods employing tomography for the generation the initial model for high resolution single particle reconstructions are also currently being used, since in most cases, finding a starting model for the averaging process is difficult.

On the other hand, when more than a 500 nm thickness of biological material is observed by cryo-EM, electron inelastic scattering is high enough to prevent the formation of a clear and informative image. In those cases, cryo-sectioning before cryo-EM of the samples is the method of choice (McDowall et al., 1983).

7.2 Results

7.2.1 Cryo-electron tomography of *M. genitalium* WT strain

Vitrified *M. genitalium* cells were subjected to CET. High quality tomograms were obtained from 0 to -15 defocus[6]. (Fig. 4.1) The nap complex, the cytoskeleton—containing the terminal button, segmented paired plates and wheel complex—, the cell membrane and some macromolecular complexes within the cell are clearly observed. Once vitrified, cells showed a thickness around 250 nm, suggesting that the cells were squeezed during the process.

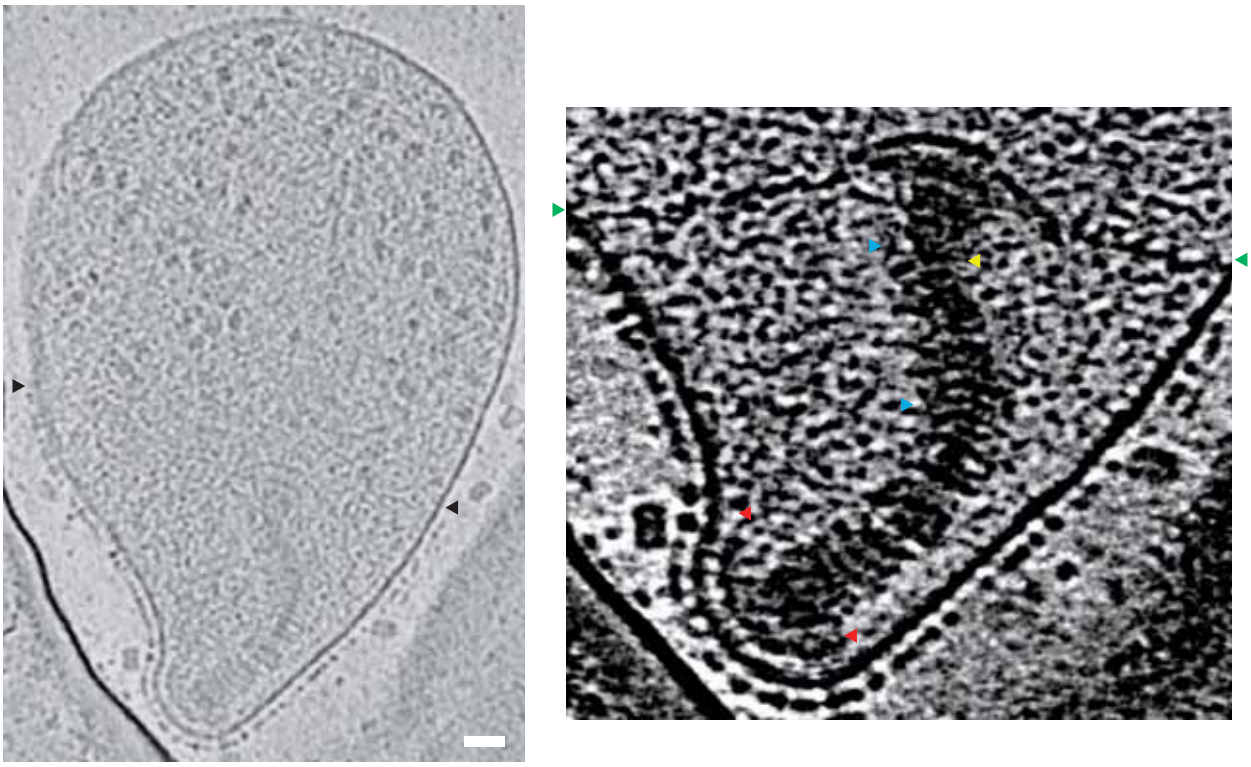

Figure 4.1. Representative cell of wild-type G37 strain. Average projection of fifteen 0.85 nm thick slices. **A.** Scale bar is 35 nm. **B.** False contrast-enhanced zoomed image of the terminal organelle in A. The terminal organelle features have been artificially highlighted to simplify their visualization. Black arrows delimitates the nap complex surrounding the terminal organelle. Red arrow indicate the interphase of the terminal button with the segmented paired plates. Yellow arrow indicates the frontier between the segmented paired plates and the wheel complex. A green arrow highlights a novel structure connecting the wheel complex with the cell membrane. Blue arrows indicate the beginning and the end of low contrast feature over half of the central rod.

[6] This is the set defocus to the microscope, real defocus may vary. Since the defocus is really measured some microns away from the sample to avoid radiation damage, it is possible that the uneven surface were the specimen lies causes variations in the real defocus. Moreover, since the microscope software is configured to maintain defocus at the carbon film height, the thickness of the sample create a fixed amount of bias in the defocus.

The nap complex is clustered around the cell membrane surrounding the cytoskeleton, completely covering the membrane of this subcellular location. Noteworthy is the fact that no macromolecular complexes are found around cytoskeleton in all cells analysed.

The cytoskeleton showed a very similar morphology that the one observed previously by CET in *M. pneumoniae*. Starting from the most distal part to the cell body, the terminal button seems to be connected to the cell membrane and, immediately after it, a rod with stripes—also known as segmented paired plates—is visible. The rod ends with wheel-like structure and so the terminal organelle.

Strikingly, when carefully analysing the area surrounding the terminal organelle, a thin layer around 4 nm connecting the wheel-like complex with the cell membrane is observed. Remarkably, the end of nap-covered membrane is always close the region where this layer connects with the cell membrane.

7.2.2 Subtomogram averaging of *M. genitalium* WT strain macromolecular complexes

The macromolecular complexes—around 20 nm in diameter—randomly distributed in the cell cytoplasm have been shown to be mostly ribosomes in these reconstructed volumes and lead to two different technical-oriented publications (Yu and Frangakis, 2014, Kunz and Frangakis, 2014). Subtomogram averaging ribosomes of a single cell (with around 160 particles each) lead to the determination of the structure at 3.5 nm of resolution.

Aiming to perform subtomogram averaging of the different macrolomecular complexes observed other than the ribosomes, manual selection of the nap complexes, terminal buttons, the individual stripes of the segmented paired plates and wheel-like structures we performed. Only nap complexes after membrane perpendicular preorientation (Fig. 4.2) resulted in a reliable result after subtomogram averaging from whole cells (Fig. 4.3).

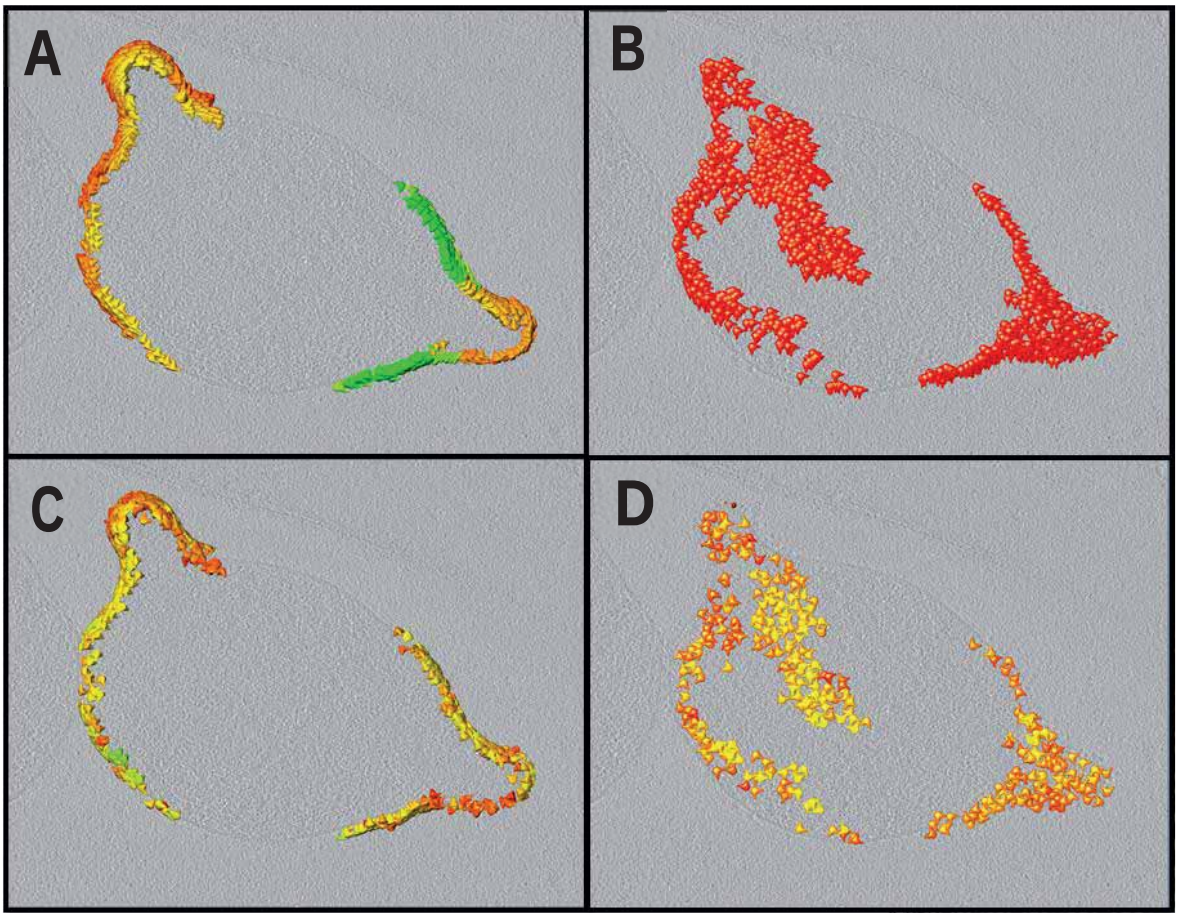

Figure 4.2. Average projection of fifteen 0.67 nm thick slices through the reconstructed volume of a WT dividing cell. **A.** Manually selected side view particles in the surface of the terminal organelle pre-oriented perpendicular to the cell membrane. **B.** Manually selected top view particles in the surface of the terminal organelle pre-oriented perpendicular to the cell membrane. **C.** Manually selected top view particles in the surface of the terminal organelle pre-oriented perpendicular to the cell membrane after subtomogram averaging. **D.** Manually selected top view particles in the surface of the terminal organelle pre-oriented perpendicular to the cell membrane after subtomogram averaging. Particle number is reduced after phi, psi and theta angle rotating and averaging due to particle clicking is not precise enough—due to low SNR and low contrast.

The nap structure resulted to be an apparent dimer of heterodimers, since it seems to be formed by 4 globular units—two of them bigger than the others—identical two by two. The diameter small subunit measures 5.5 nm and the big subunit 6.5 nm. The tetramer presents a 2-fold rotational symmetry, meaning that it is likely that the two big globular entities are likely to be the same protein (or complex) while the two small globular items are also likely to be the same. The link to the membrane is not evident, but a greater electron density is observed in the region between the bigger globular subunit and the membrane, suggesting at least two anchoring domains in the nap complex. Each small subunit is interacting with two bigger subunits and vice versa. Interestingly one of this interactions seems to be stronger or closer than the other, since the electron densities partially overlap in one of the interaction surfaces.

The globular part of the nap complex is 10 nm wide—in the tighter interaction region—11 long—in the loosely interaction region—and 8 nm high. In average, the nap seems to be at a distance of 4 nm from the outer layer of the cell membrane. Using the 0.5 Fourier shell correlation (FSC) criteria (Frank, 1996, Bottcher et al., 1997) the resolution achieved is assigned to 3.5 nm (Fig. 4.3B).

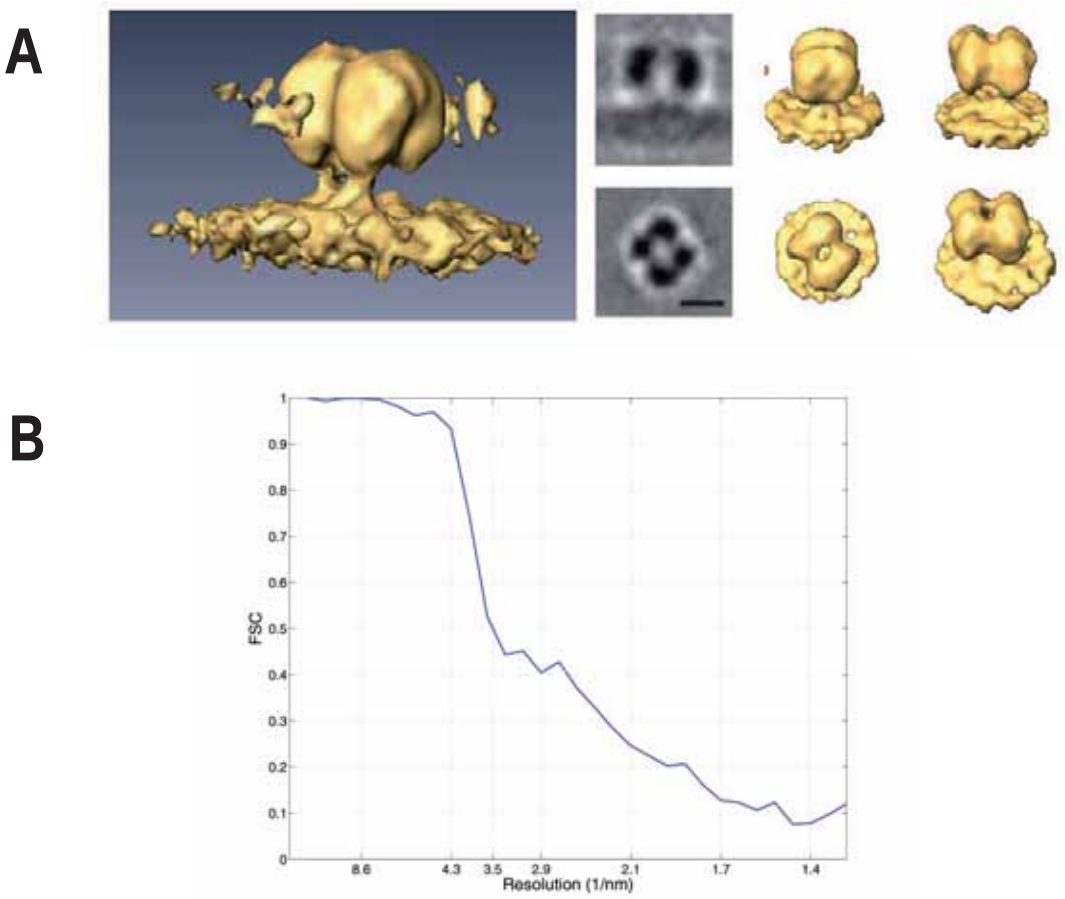

Figure 4.3. Structure determination of the nap complex by cryo-electron tomography. **A.** Electron density map obtained from the averaging (gray tones) and isosurfaces (yellow) generated from this electron density map. The isosurface was generated estimating a molecular weight of 548 kDa (the expected Mw of a tetramer composed by P110 and P140). **B.** Fourier shell correlation plot of subtomogram averaging of the nap.

Once properly aligned, the original rotational angle of the particle is known and can be positioned in the space (Fig. 4.4). This representation showed that there is no preferential orientation of the nap over the surface of *M. genitalium* cells.

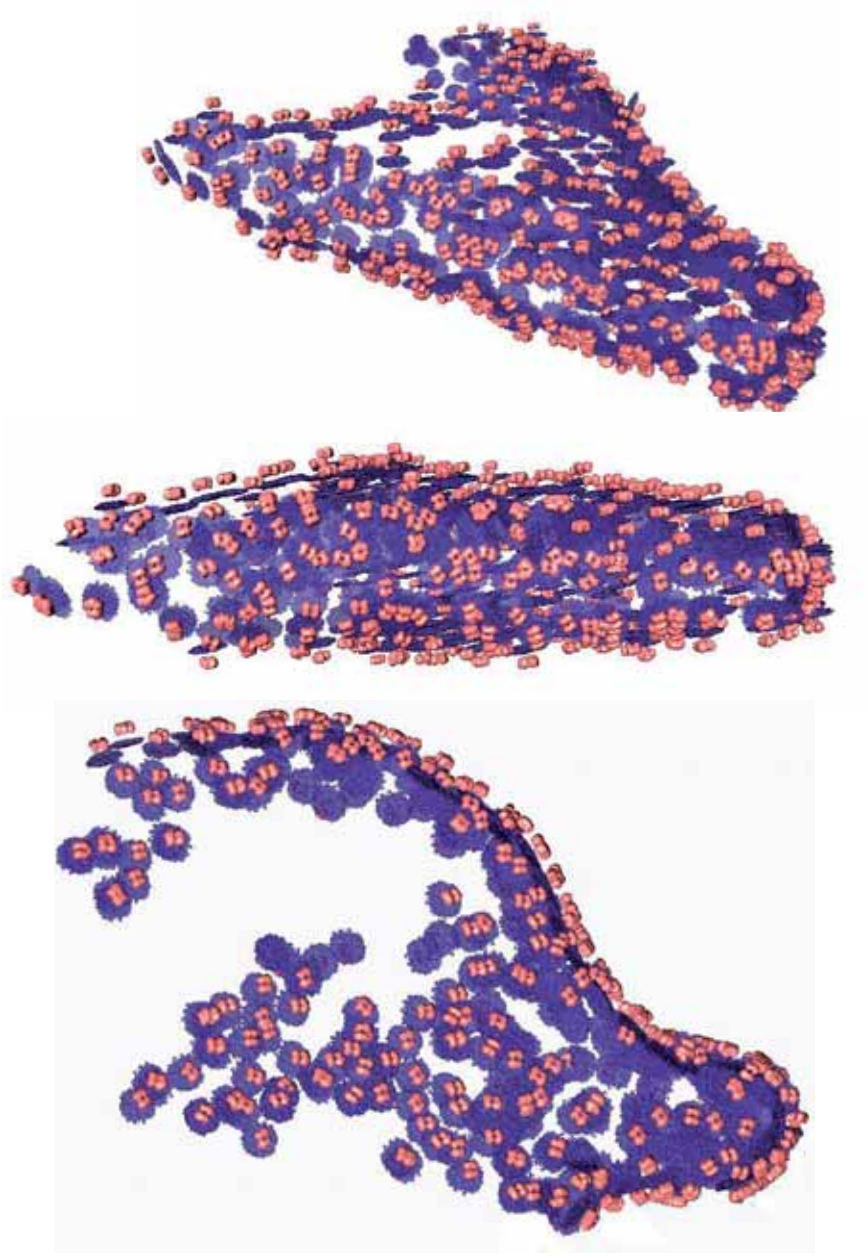

Figure 4.4. Different views of orientated naps (pale red) and the membrane immediately under it (purple) used for subtomogram averaging one one *M. genitalium* cell.

Since subtomogram averaging from the terminal button and the wheel complex from whole cells were unsuccessful, cells grown over continuous carbon films were treated with a 1% Triton X-100 to lyse the cells and analyse terminal organelles by CET. With this treatment, the sample is expected to have lower thickness and therefore better SNR. This lysed cells can be called 'ghosts' (Uenoyama and Miyata, 2005).

M. genitalium ghost cells analysed by CET resulted in high quality volumetric reconstructions (Fig. 4.5A). The cytoskeleton looked exactly identical that in whole cells, but the lack of material around the electrondense core and the thinner ice make its features more clearly visible. However, artefacts by detergent cannot be discarded. In some cases, detached organelle from the surrounding membrane is observed. A small structure under the nap in ghosts cells can be observed (Fig. 4.5B) as previously shown in *M. pneumoniae*. Nap structures are also more easily visualized in ghosts and—in agreement with spatial positioning of the averaged naps—seem not to be organized in any preferential position.

Longer treatments with triton X-100 or adding centrifugation steps before applying the ghosts into the grid allowed the purification of cytoskeleton without membranes, but the quality[7] of the reconstructions obtained was not good enough to be analysed (data not shown).

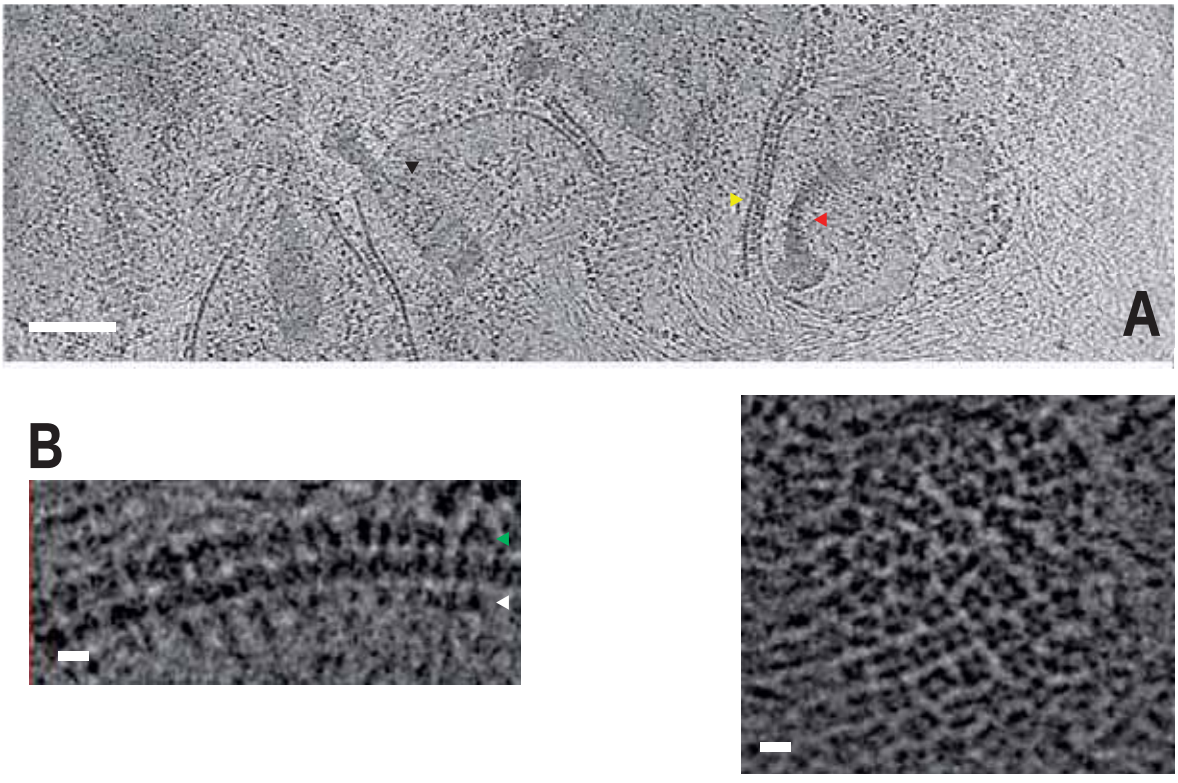

Figure 4.5. Average projection of fifteen 0.85 nm thick slices through the reconstructed volume of G37 ghost cells. **A.** General view of ghost cells of *M. genitalium.* Black arrow indicates a top view of the cytoskeleton. Red arrow points a side view of the terminal organelle. Scale bar 100 nm. **B.** Withe arrow indicates a ~5 nm globular structure under the nap (green arrow). Scale bar 10 nm. **C.** Top view of the nap complexes of the WT ghost cells. Scale bar 10 nm.

[7] Cytoskeletons and DNA seems to be strongly interacting. This resulted in an extremely high viscous sample, with difficult the blotting for thin ice and the proper mixture of the fiducial markers added. This resulted in a bad alignment and poor SNR. Treatment with DNAse is the most reasonable improvement, but since ghost cells produced with mycoplasmas grown over the grid give good results, this protocol was no further optimized.

A small number (20 of each) terminal buttons and wheel-like complexes were manually clicked and roughly averaged with PyTom (Hrabe et al., 2012). Wheel-like complexes averaging failed to give any reliable result, but the terminal button averages resulted in a trustworthy result (Fig. 4.6) but no resolution could be estimated from that reduced number of particles. No assessment of the resolution achieved can be done by two major reasons; the small number of particles analysed and the preferred orientation for top views of the terminal organelle in the sample. Subtomobram averaging of the segmented paired plates or the whole cytoskeleton was not attempted since the expected flexibility of the structure would lead no averaging results.

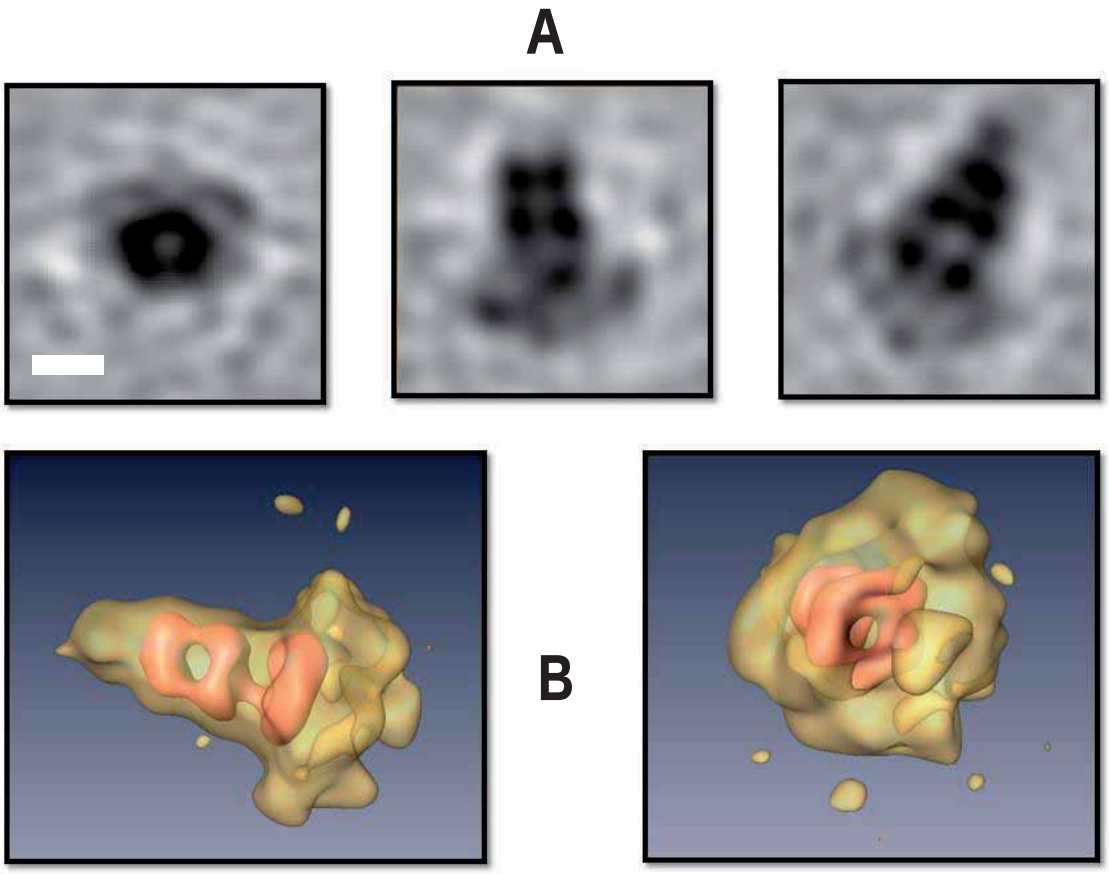

Figure 4.6. Low resolution structure of the subtomogram averaging resulting from 20 terminal buttons **A.** Electron density map obtained from the averaging (gray tones) and Scale bar 20 nm. **B.** Isosurfaces (yellow and red) generated from the electron density map in A.

7.2.3 Isolation and structural characterization of the adhesion complex of *M. genitalium*

Since P110 and P140 are supposed to be the main adhesins of *M. genitalium* and localizes in the surface of the terminal organelle, it is reasonable to hypothesize that the four globular entities forming the nap complex are P110 and P140. In order to demonstrate that a single particle reconstruction experiment was designed.

Using a previously mutant obtained in our lab[8] carrying an extra copy of P110 with a 6 histidine tag in its C-terminal an IMAC purification was performed. OG was selected as the detergent to extract adhesion complexes from the membrane since P1 and P90 have been previously solubilized in *M. pneumoniae* (Nakane et al., 2011). Luckily, P110 and P140 are so strongly interacting that an equimolar quantity of both proteins are obtained when purified from *M. genitalium* cells by affinity cromatrography (Fig. 4.7).

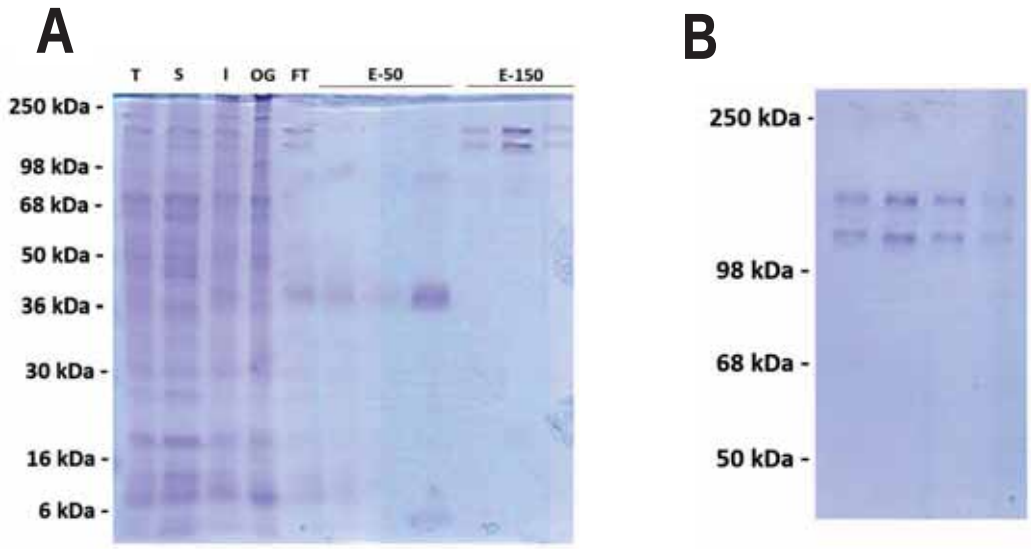

Figure 4.7. Isolation and purification of P110 and P140 (nap complex). **A.**SDS-PAGE of the purification process of P110 and P140. M: Molecular weight marker, T: Total cell lysate, SF: Soluble fraction after sonication, I: Insoluble fraction after sonication, OG: Solubilized proteins from the insoluble fraction with OG. FT: follow-through; non retained protein in the IMAC column, E-50: eluted fraction with 50 mM imidazole. E-150: eluted fraction with 150 mM imidazole. Densitometry analyses showed a purity of 99% prior to the size exclusion chromatography. **B.** SDS-PAGE of the only UV-detected peak detected after size exclusion chromatography of P110 and P140 complex isolated by affinity chromatography. The different lanes correspond to 0.5 ml fractions of the same peak. The migration behaviour of the particle within the column correspond to an approximate size of 440 kDa.

Size exclusion chromatography (in comparison with different Mw known proteins) of the purified P110 and P140 complex revealed that the estimation of size of the complex is around 440 kDa. This peak was symmetrical, suggesting the homogeneity and purity of the peak. No

[8] Burgos, R. unpublished results. This strain carries (within two IRs) a TetM438 and a C-ter translational fusion of MG_192 gene product with six histidine residues. The insertion point of this construct is base 489735—in the forward strand between MG_386 and MG_387.

peak was observed in void volume of the column, suggesting no aggregation of the particles. It is important to note that detergents can affect—depending on the size of its micelle—the migration of proteins in size exclusion chromatography, thus showing an apparent molecular different Mw than expected (Kunji et al., 2008).

Serial dilutions of the 500 kDa eluted complex of P110 and P140 were negatively stained with uranyl acetated dried and observed in a TEM microscope (Fig. 4.8).

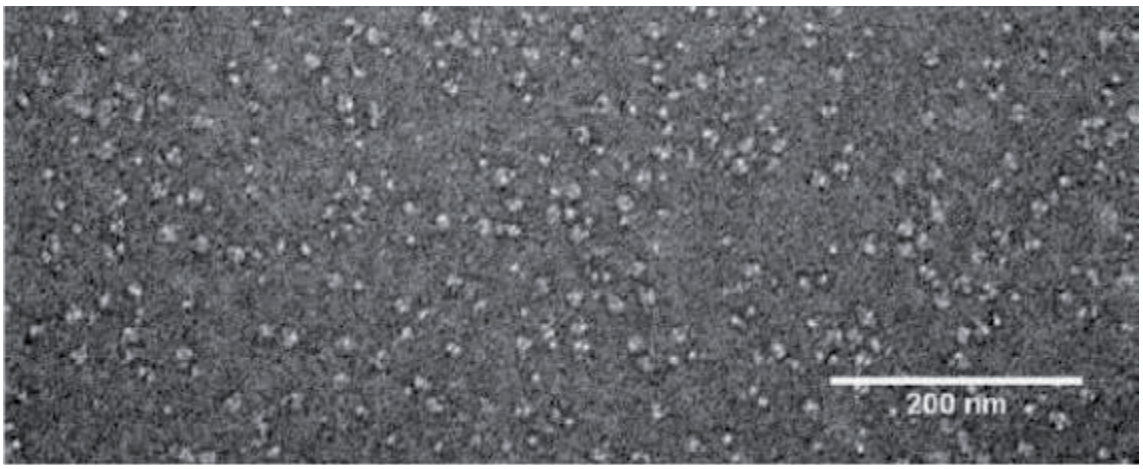

Figure 4.8. Negative staining electron micropagh of the P110 and p140 purified from *M. genitalium*.

The highest dilution tested resulted in a grid with multiple macromolecular complexes between 5–20 nm. A total of 19835 particles where manually picked and were classified in 30 different dissimilar 2D projections (Fig. 4.9).

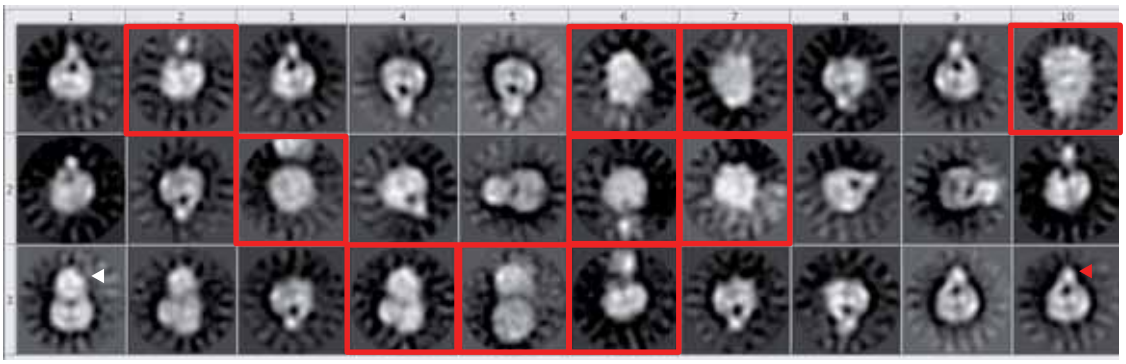

Figure 4.9. Different 2D projections of P110 and P140 purification using CL2D. Red and white arrows indicate small and big putative OG micelles respectively. Highlighted classes in red were discarded for further processing.

Particle classification revealed that three major types or particles can be observed: an almost circular 2D projection (e.g. position 2:7), a flattened sphere connected with one or two sticks to a small sphere (e.g. position 3:10), and a projection with a flattened sphere with a big sphere (e.g. position 3:1). The circular projections are top views or—most likely— aggregates of P110 and P140 and were not further considered. Taking in account that the samples are almost at OG's CMC is it possible that different sized spheres are micelles of OG[9]. This would indicate that the arrows in Fig. 55 point to the transmembrane regions of P110 and P140 surrounded by detergent molecules.

The averaging was continued only with classes similar to 3:10 and 3:1, leaving 14375 particles in the dataset. Those classes were further 3D clustered in 4 different classes (Fig. 4 .10B) with the help of a ball-and-stick model generated with 2000 particles vertically aligned and 90 degrees rotated and later filtrated to 6 nm (Fig. 4.10A). Those four classes were judged as different orientations of the same particle and combined for the final averaging. The process resulted in one structure (Fig. 4.11). The resolution achieved is estimated to be 1.9 nm— using SNR criteria in RELION software (Scheres, 2012b, Scheres, 2012a).

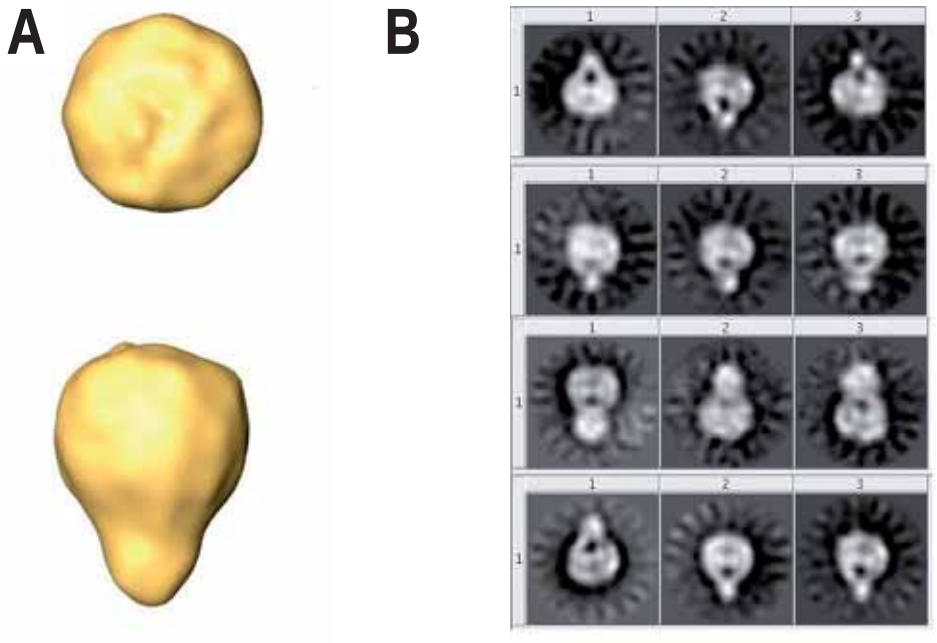

Figure 4.10. Preliminary volumes and classifications generated for P110 and P140 image processing. **A.** Initial model generated for later averaging. **B.** 2D classification of the images of the four 3D classes.

[9] Micelles of OG form in concentration greater than 0.53% (w/v). The sizes of the micelles are 2-8 nm. VINSON, P. K., TALMON, Y. & WALTER, A. 1989. Vesicle-Micelle Transition of Phosphatidylcholine and Octyl Glucoside Elucidated by Cryo-Transmission Electron-Microscopy. *Biophysical Journal,* 56**,** 669-681.

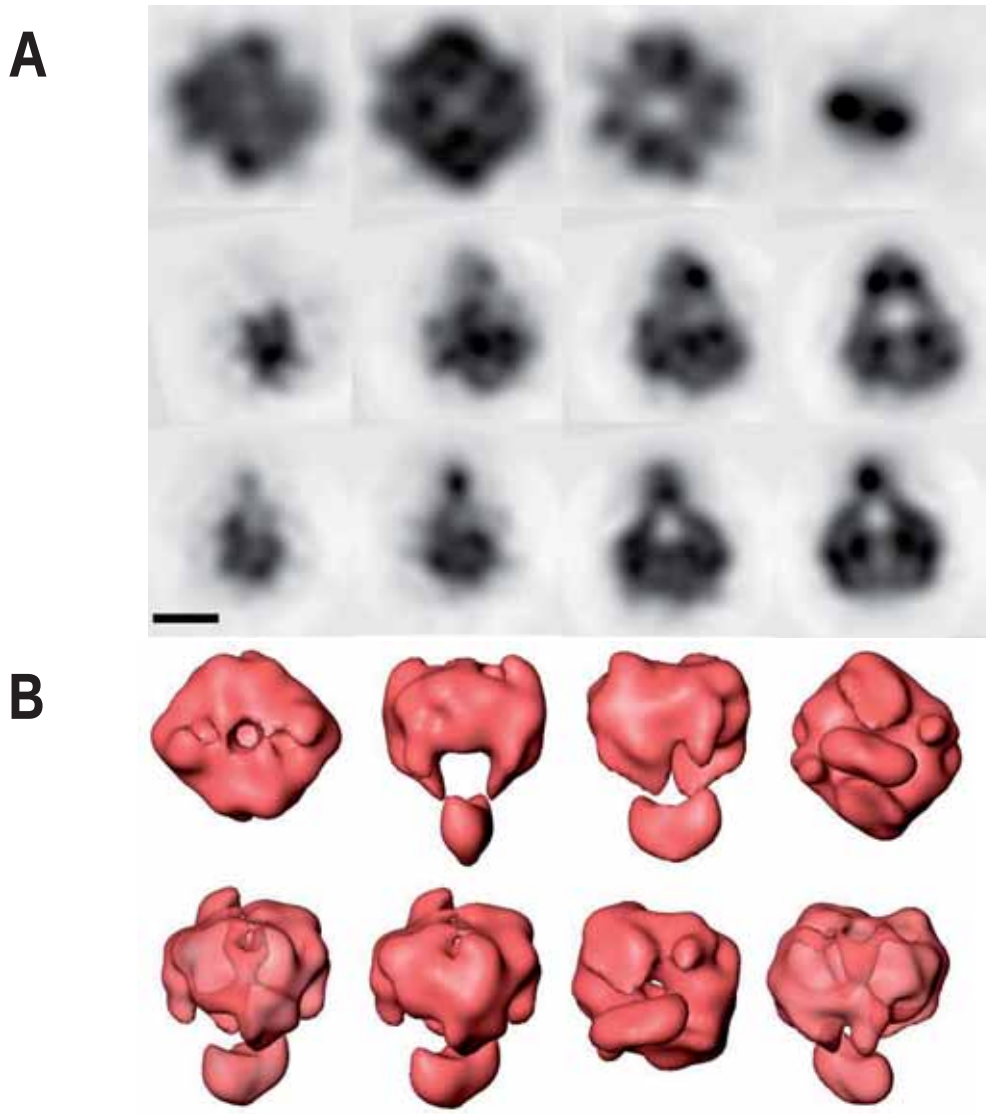

Figure 4.11. 3D refined structure from the 2D projections obtained by negative staining TEM of P110 and P140. **A.** Consecutive slices from different directions of the electrondensity obtained from single particle averaging. First row are different consecutive Z slices of the complex. Second row are different consecutive Y slices of the complex. Third row are different consecutive X slices of the complex. Scale bar is 5 nm
B. Different views of the isosurface generated with the electrondensity resulted from the averaging.

The globular part of the P110-P140 complex is 10 nm wide, 11 long, and 14 nm high. This globular part presents a central hole of 2.1 nm in diameter—creating a channel through the whole particle till the transmembrane region. This transmembrane region is connected to the globular part of the complex by four stick-like structures—two of them bigger than the other two. The relative big size of the transmembrane regions are compatible with the presence of detergent in addition to the transmembrane regions. The surface of the side opposite to the transmembrane region (which should be the most accessible surface of the particle to the extracellular medium) presents a groove of 1.5 nm diameter that contains a 0.6 nm. Given the limited resolution achieved in the reconstruction, this small features should be taken with caution.

7.2.4 Cryo-electron tomography of MG191 and MG192 null mutants

CET of the null mutant lacking P110 and P140 main adhesins (strains mg191⁻ and mg192⁻) showed a high frequency of bigger cells than the wild-type strain—almost all of them. mg191⁻ and mg192⁻ cells lack the characteristic flask-shape morphology. Generally, cells analysed presented a completely normal cytoskeleton (terminal button attached to the membrane, rod and wheel complex), but a 20% of them lack any form of cytoskeleton. In fact, is common to find cells with multiple terminal organelles (Fig. 4.12). Noteworthy is the presence of a much clearer electron lucent area in this strains than in the wild-type strain (Fig. 4.12B).No cells attached to the holey carbon surface were observed.

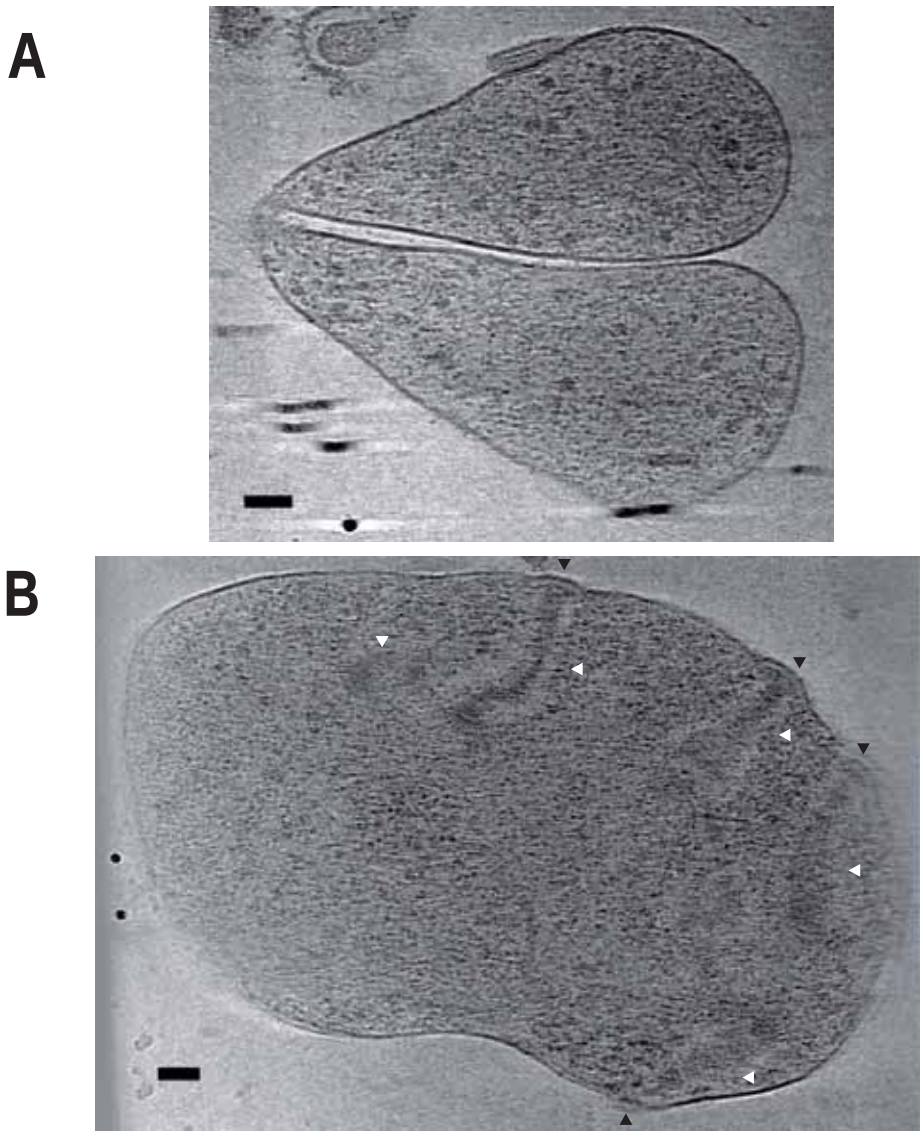

Figure 4.12. Average projection of fifteen 0.67 nm thick slices, obtained by CET, through the reconstructed volume of mg191⁻ and mg192⁻ cells. **A.** Example of a mg192⁻ cell without cytoskeleton. **B.** Composite image of difference Z slices of big a mg192⁻ cell with multiple cytoskeletons. White arrows point cytoskeletons (top or side view). Black arrows point to a characteristic protuberance formed in the region where terminal button interacts with the cell membrane. Scale bar is 50 nm.

7.2.5 Cryo-electron tomography of MG_312 and MG_218 null mutant

CET of cells of both ΔMG_312 and ΔMG218 mutants showed no cytoskeleton of any kind or other macromolecular complexes rather than the ribosomes and small amounts of nap complex (Fig. 4.13).

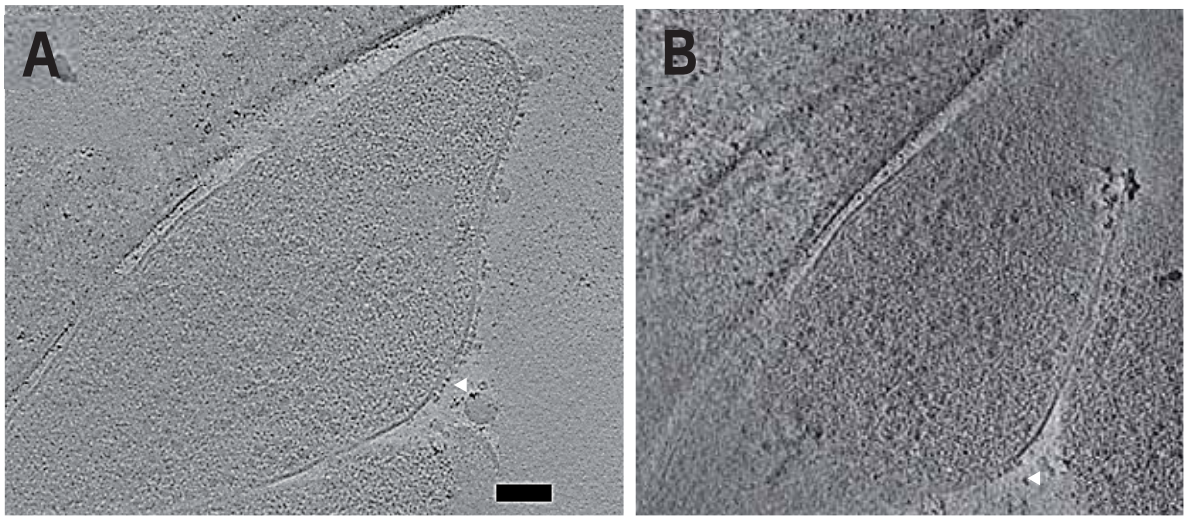

Figure 4.13. Average projection of fifteen 0.85 nm thick slices, obtained by CET, through the reconstructed volume of ΔMG312 cell. **A.** Composite image of different Z slices of a cell of ΔMG_312 cell. **B.** ΔMG218 cell. White arrow points to nap complexes. Scale bar is 80 nm.

7.2.6 Cryo-electron tomography of MG217 null mutant

Cells of strain ΔMG_217 showed presented flask-shape morphology and a cytoskeleton with all its components (Fig. 4.14). Strikingly, the size of the terminal button in cells of this strain was significantly smaller than in the WT strain (Fig. 4.15). The terminal button size was stablished by its diameter from its most distal part from the membrane. Terminal button from wild-type cells measures 63.1 ± 1.3 nm and the ΔMG_217 terminal button measured 54.7 ± 1.1.

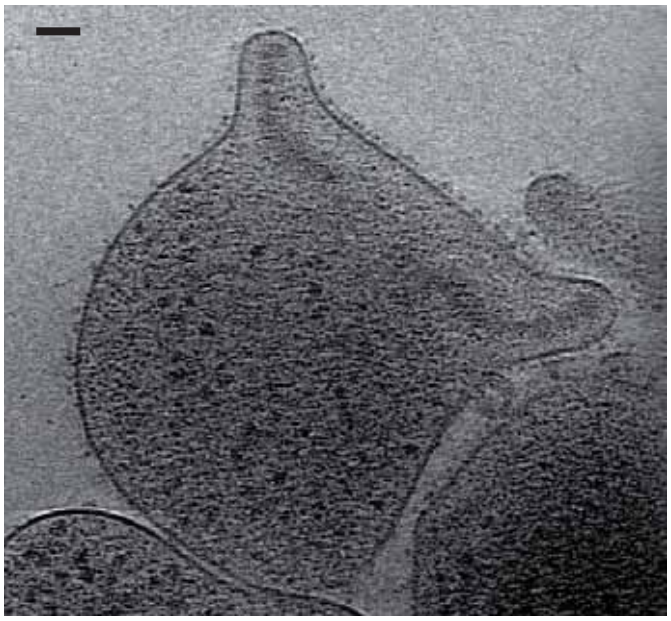

Figure 4.14. Average projection of fifteen 0.67 nm thick slices, obtained by CET, through the reconstructed volume of ΔMG_217 cell in division. Scale bar is 50 nm.

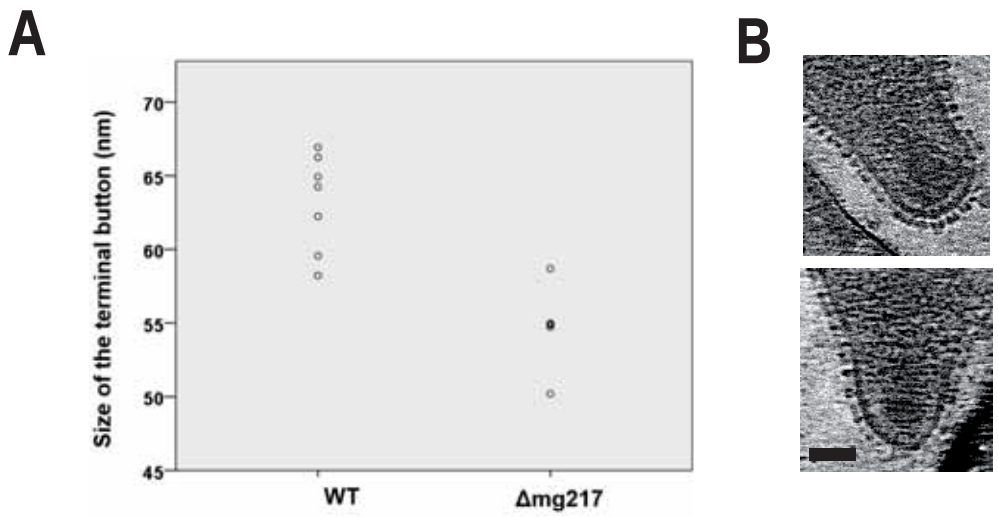

Figure 4.15. Terminal button size of Δmg217 and G37 cells. **A.** Size distribution of the width of the terminal button. **B.** Upper panel: G37 WT terminal button. Lower panel: Δmg217 mutant terminal button. Scale bar is 50 nm.

7.2.7 Cryo-electron tomography of MG317 null mutant

Mutants from strain lacking the entire MG_317[10] locus were analysed by CET. No cells with standard terminal organelle were observed. ΔMG_317 cells neither showed terminal button, nor segmented paired plates, nor wheel-like complex. However, ΔMG_317 cells presented a completely aberrant the cytoskeleton (Fig. 4.16). An important number of filaments joining two cells were recovered with nap complexes. Moreover, in some cases (14%), cells presented the electron dense core in the opposite cell pole to the expected (right panel in Fig. 4.16).

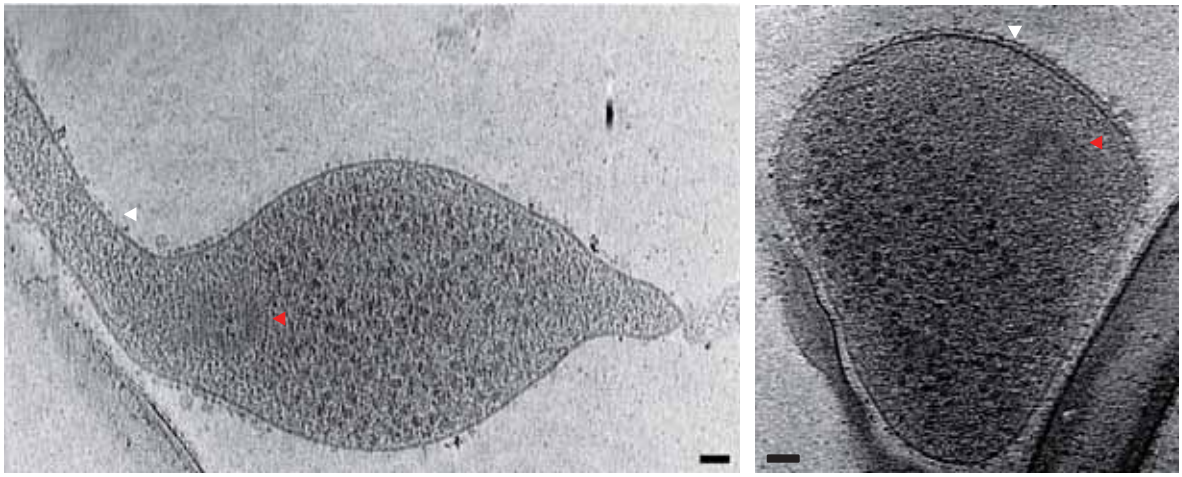

Figure 4.16. Two different average projections, obtained by CET, of fifteen 0.67 nm thick slices through the reconstructed volume of Δmg317 cells. Scale bar is 50 nm. White arrows point to nap complexes. Red arrows indicate abnormal electron dense cores.

[10] The ΔMG_317 strain was previously obtained in our lab. (Pich, OQ, unpublished results).

7.2.8 Cryo-electron tomography of MG491 mutants

Cells from Δmg491 strain present a pleomorphic morphology and often terminal organelles protruding from the cell body or aggregates (Fig. 4.17). Infrequently, detached terminal organelles from the cell body can be observed.

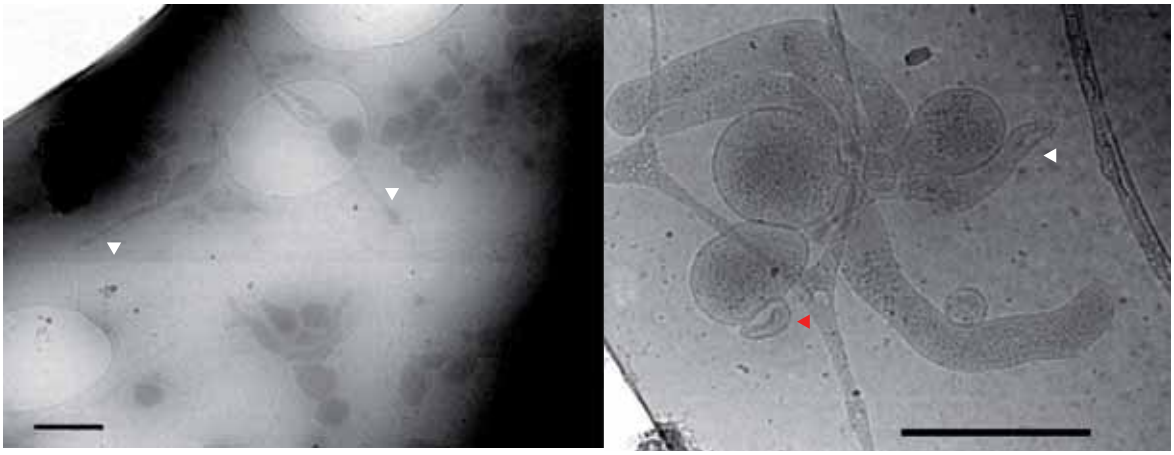

Figure 4.17. Cryo-EM image of Δmg491. White arrows point to terminal organelles in process of detachment. Red arrows point to a detached terminal organelle. Scale bar is 1 µm.

CET of Δmg491 cells revealed that protruding filaments or detached terminal organelles contain a cytoskeleton composed by terminal button and segmented paired plates (Fig. 4.18). No wheel-like complex have been observed in any of the cells analysed. Occasionally, the segmented paired plates are longer than in the WT strain in rare occasions (Fig. 4.18B and 4.18C). The detached terminal organelles sometimes contain only the terminal organelle itself (Fig. 4.18B) or also cytoplasmic material and can be considered minute cells (Fig. 4.18A). Detached terminal organelles—and some minute cells—where completely recovered with nap complexes. The rod length is the expected for a cytoskeleton lacking the wheel-like complex.

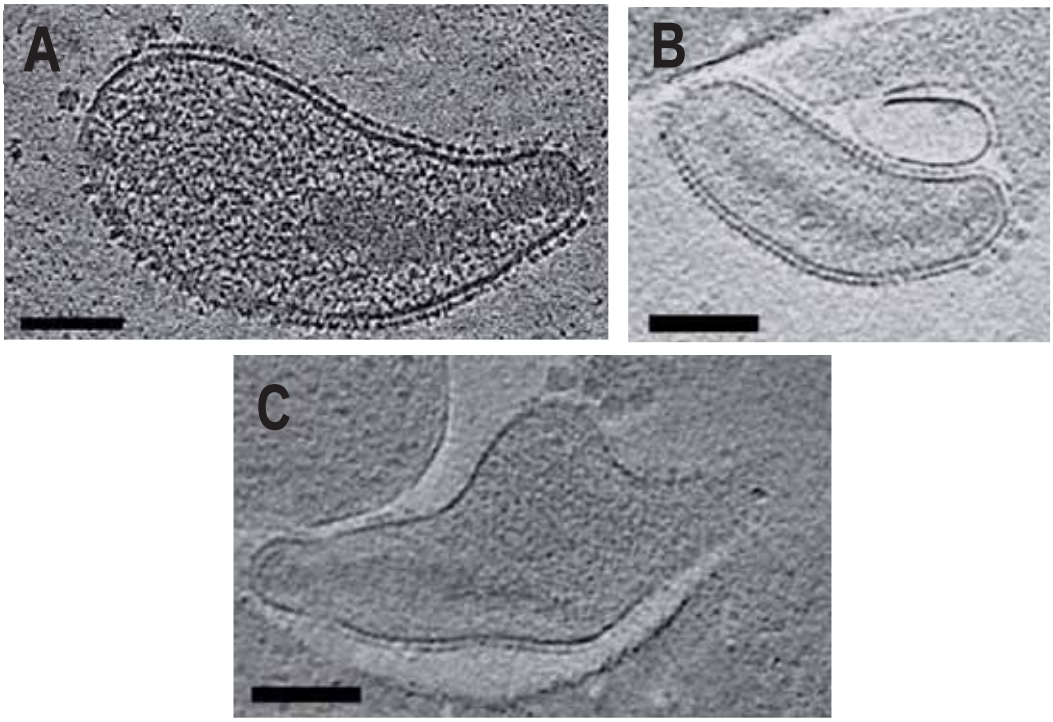

Figure 4.18. Average projection of fifteen 0.85 nm thick slices through the reconstructed volume of Δmg491 cells. Scale bar is 100 nm. **A.** Minute cell. **B**. Composite image of different Z slices of detached terminal organelle. **C.** Composite image of different Z slices of a cell of Δmg491 protruding filament prior to detachment.

7.2.9 Cryo-electron tomography of MG200 null mutant

CET analyses of a mutant lacking the C-terminal and APR domain of MG200 (GD clone 12) revealed that the C-terminal of MG200 is not critical for any of the structures of the terminal organelle (Fig. 4.19A) because it presents a WT cytoskeleton. However, it is important that almost all of the cells analysed (80%) presented a cytoskeleton in duplication process or more than one cytoskeleton (Fig. 4.19B).

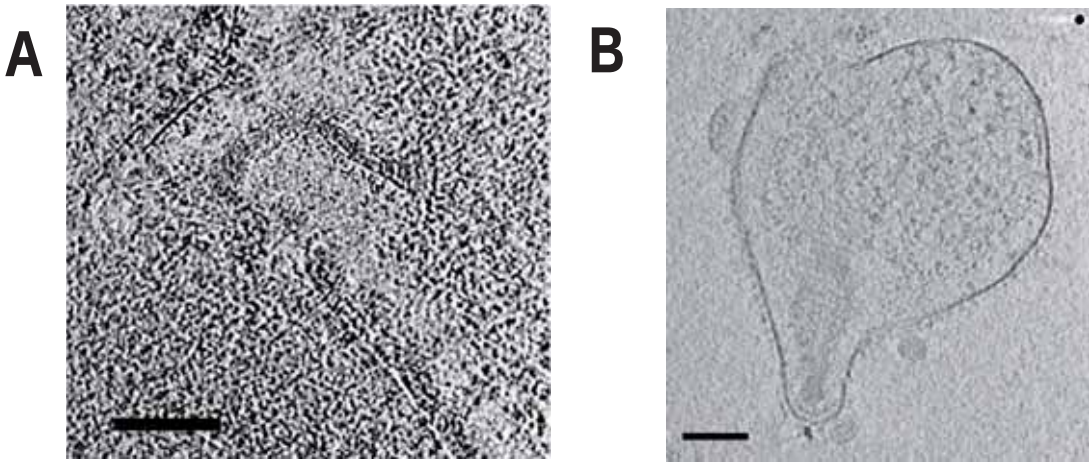

Figure 4.19. Average projection of fifteen 0.67 nm thick slices through the reconstructed volume of GD clone 12 cells with terminal organelle. **A.** Composite image of different Z slices of a cell with abnormal terminal organelle. **B.** Composite image of different Z slices of a lysed GD clone 12 cell. This cell present two rods but only one terminal button.

7.2.10 Cryo-electron tomography of MG386 mutants

CET of GD clone 23—a transposon mutant expressing only the first third of MG386—revealed no major differences in the composition and structure of the cytoskeleton. Nevertheless, when carefully analysing the curvature of the rod a striking difference was found. GD clone 23 cells presented an extra bent in the rod when compared with the WT, affecting the curvature angle of the cytoskeleton (Fig. 4.20).

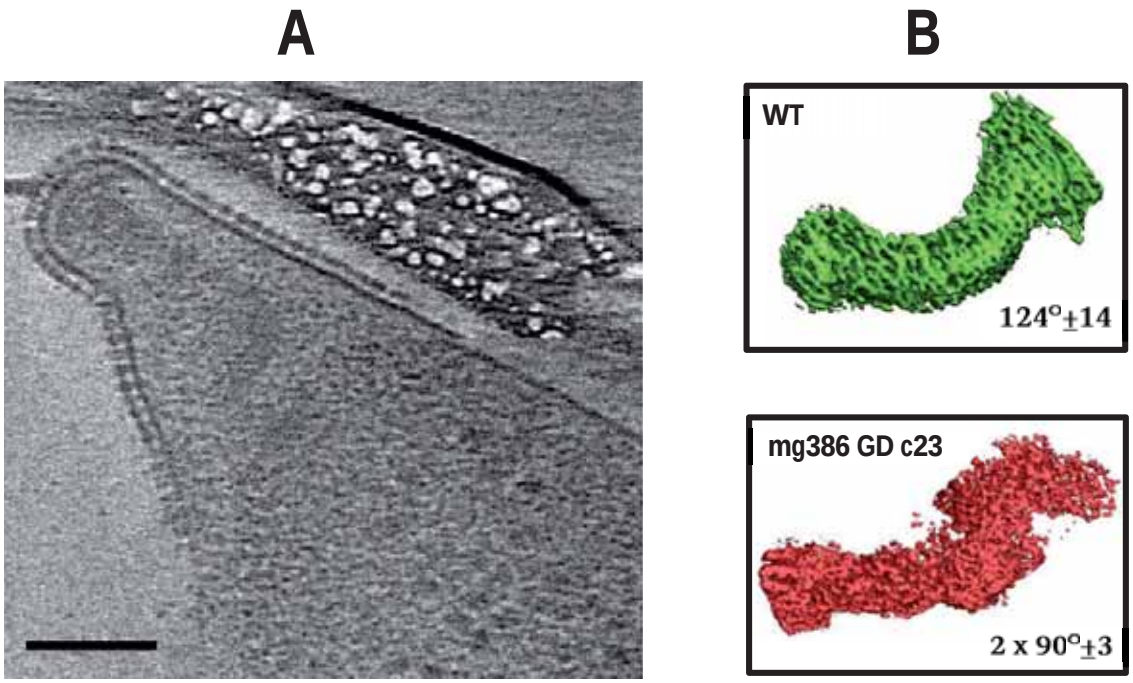

Figure 4.20. Average projection of fifteen 0.67 nm thick slices through the reconstructed volume of GD clone 23 cells with terminal organelle. **A.** Section of a terminal organelle of an intact cell. **B**. Upper panel: Isosurface generated with the 3D segmentation of WT cytoskeleton (in Fig.4.1A). Lower panel: Isosurface generated with the 3D segmentation of the cytoskeleton in A. Scale bar is 100 nm.

Cryo-EM analyses of a mutant lacking the entire of coding region for MG386 showed protruding filaments from the cell body containing the cytoskeleton of the terminal organelle (Fig. 4.21).

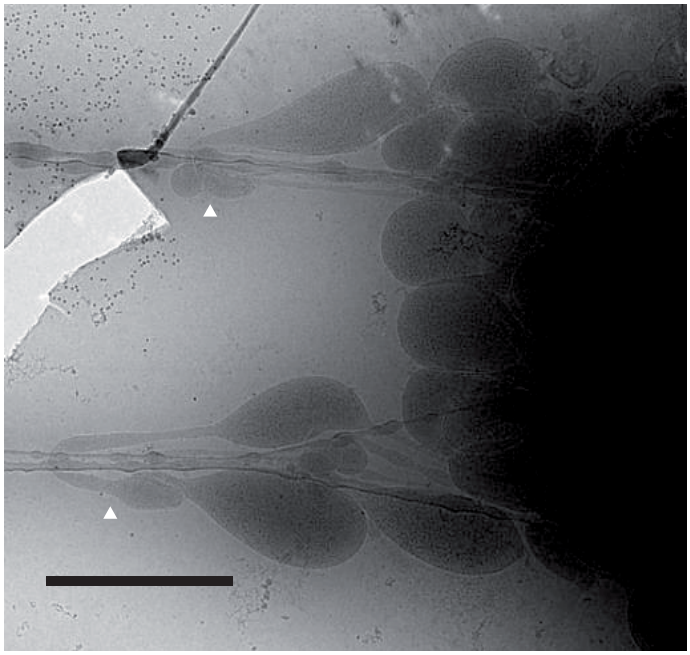

Figure 4.21. Cryo-EM image of ΔMG386. White arrows point to terminal organelles in process of detachment. Scale bar is 1 μm.

In addition, CET analyses of the terminal organelles in ΔMG386 strain, showed that the nap complexes localized only on the cell membrane surrounding the cytoskeleton (Fig. 4.22). No wheel complex can be observed in any of the reconstructed volumes of ΔMG386 cells. The rod length is the expected for a cytoskeleton lacking the wheel-like complex.

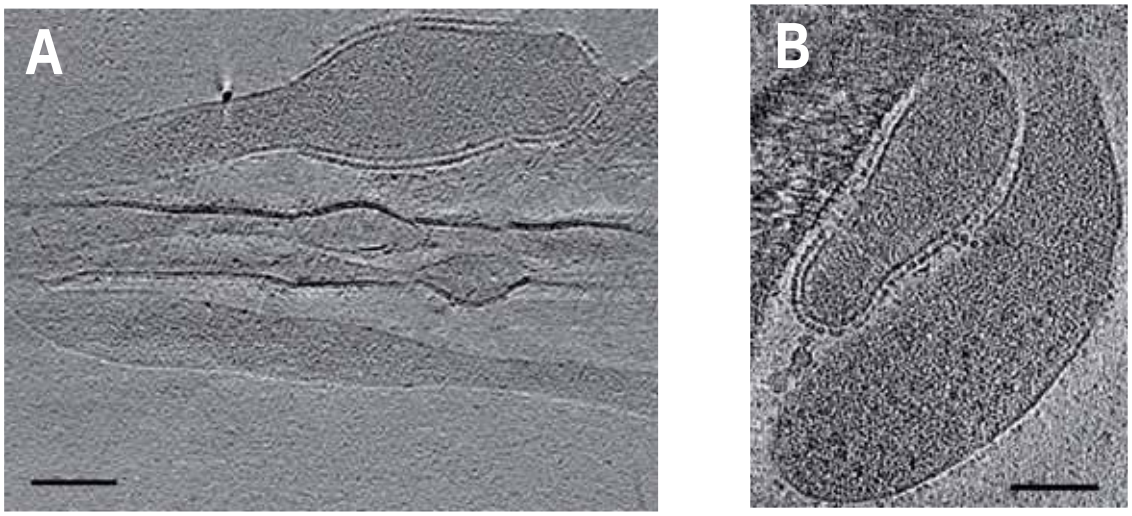

Figure 4.22. Average projection of fifteen 0.67 nm thick slices through the reconstructed volume of Δmg491 cells with terminal organelle. Both are composite image of different Z slices of a cell with terminal organelles in process of detachment. **A.** Top view of a detaching terminal organelle. **B**. Side view of a detaching terminal organelle. Scale bar is 100 nm.

7.2.11 Cryo-electron tomography of MG318 mutants

ΔMG318 and ΔMG318C-ter showed the same morphology when analysed by CET (Fig. 4.23). Interestingly, the 88 % of the cells analysed showed an unaligned terminal button relative to the cell membrane (Fig. 4.23A and 4.23C). The terminal button instead of being out protruding of the cell body is within the cell, suggesting the improper distribution of the components of the terminal organelle in the absence of P32. Moreover, macromolecular complexes near the adjacent to the cytoskeleton can also be observed (Fig. 4.23C). In all cases, the terminal button exhibited a smaller size than the WT strain (Fig. 4.23D). Terminal button from wild-type cells measures 63.1 ± 1.3 nm and the ΔMG_386 terminal button measured 53.5 ± 2.6.

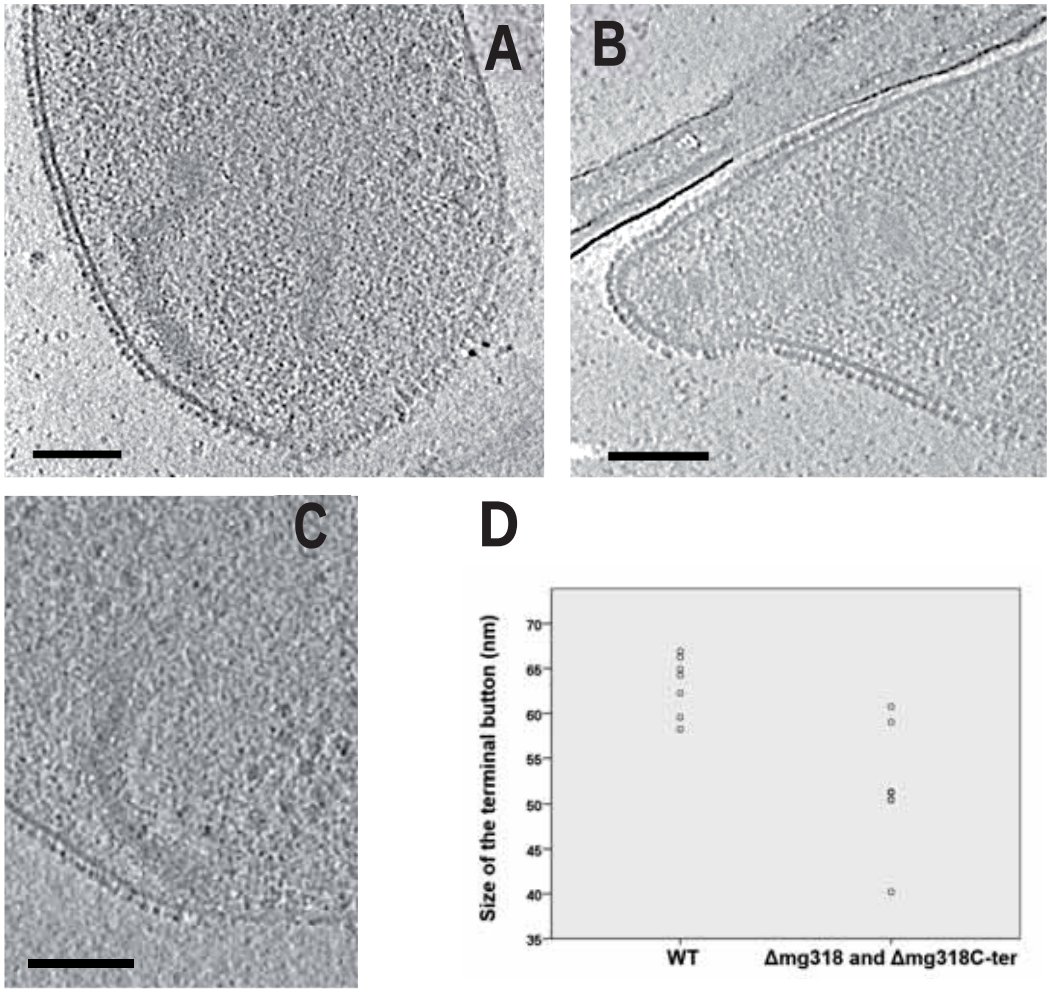

Figure 4.23. Average projection of fifteen 0.85 nm thick slices through the reconstructed volume of ΔMG318 mutant cells. **A.** ΔMG318 cell which terminal organelle side view which terminal button is not aligned properly with the cell membrane **B**. ΔMG318 top view of a terminal organelle with a properly aligned terminal button. **C**. ΔMG318C-ter terminal organelle side view which terminal button is not aligned properly with the cell membrane Scale bar is 100 nm. **D.** Size distribution of the width of the terminal button.

7.2.12 Cryo-electron tomography of MG219 mutant

ΔMG219 cells showed no differences in the cytoskeleton or the terminal organelle when compared with the WT (Fig. 4.24).

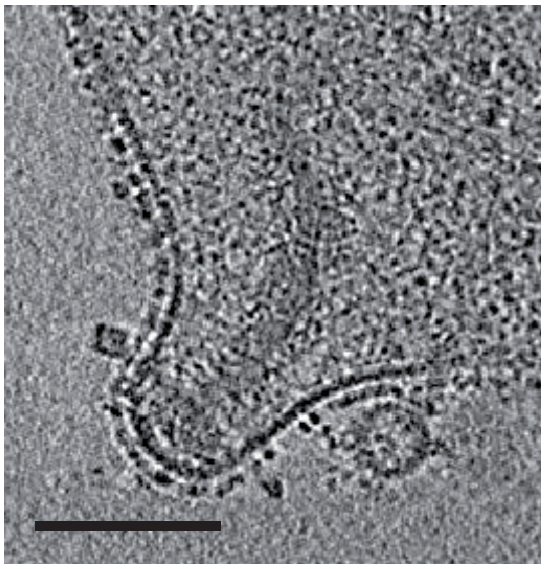

Figure 4.24. Average projection of fifteen 0.85 nm thick slices through the reconstructed volume of ΔMG219 cells. Scale bar is 100 nm.

7.2.13 Cryo-electron tomography of MD-P3 mutant

Mutant lacking the expression of the C-terminal independent fragment of MG218 (MG218-s) did not show significant differences in the terminal organelle or the cytoskeleton of its cells (Fig. 4.25).

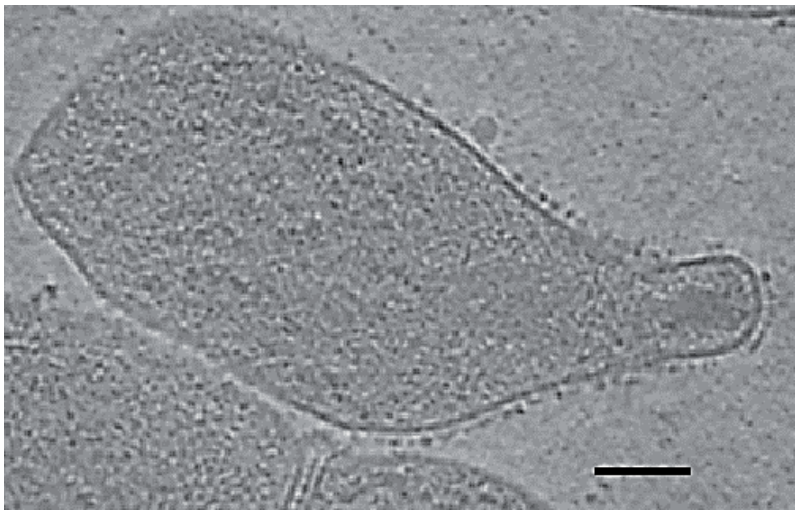

Figure 4.25. Average projection of fifteen 0.85 nm thick slices through the reconstructed volume of MD-P3 cells. Scale bar is 100 nm.

7.3 Discussion

Cryo-electron tomography have been proven useful for the study of the macromolecular complexes of *M. genitalium*. The nap, the cytoskeleton—and its forming parts: the terminal button, the segmented paired plates, and the wheel-like complex—shown to be clearly visible.

The terminal button seems to be a bowl-shaped structure interacting with the membrane to the most distal part relative to the cell body. Immediately after, a segmented rod than no les of 18 'stripes' and around 400 nm in length is present. Subtomogran averaging of the terminal button showed that stripes are side views of ring structures. It is not risky to hypothesize that the entire rod is formed by rings instead of plates—as suggested in *M. pneumoniae*. In this organism, the rod is called segmented paired plates because a thin and a thick plates are clearly distinguishable. However, a differentiated electrondensity side-by-side of the rod can be intuited. In short, the thin plates are not obvious in *M. genitalium*. Is it possible that the thin plates does not exists in *M. genitalium* or that the thin plates exist but they closer to the 'thick plates' than in *M.* pneumoniae, making impossible to discern this two structures. It is also possible that the clearer electronlucent area around *M. pneumoiae* cytoskeleton makes much easier to distinguish this structures. Given the unknown protein nature of the thin plates, it is impossible to further discuss this matter.

At the end of the rod, the wheel-like complex is present and seems to be formed by a pyramidal structure followed by another bowl-like complex. The curvature of the wheel-like complex is less pronounced than in the terminal button. At the end of the wheel-like complex, a membrane-like structure around 4 nm thick is visible in most of the reconstructed volumes of whole cells of the WT strain. This lamellar structure connects the wheel-like complex with the most distal part, relative to the terminal button, of the cell membrane linked to the terminal organelle. It is most likely that the structure responsible for the separation of macromolecular complexes (*e.g.* ribosomes) from the area surrounding the terminal organelle cytoskeleton. It is unknown if this separation is the real function of this structure or just a consequence of its location, an active function in gliding motility cannot be discarded.

Interestingly, the high quality of the tomograms acquired in addition to the great number of nap complexes surrounding the membrane of the terminal organelle lead to the determination of the nap structure at 3.5 nm by subtomogram averaging. The nap showed to be composed apparently by 4 globular molecules (2 x 6 nm and 2 x 5 nm), with one strong and one tight interacting regions for each molecule, each small particle interacting with two

big particles and vice versa. The heterodimer is 10 in length suggesting that 0.5 nm of each particle overlap in when tightly interacting.

Since it has been long suggested that P110 and P140 are the major surface antigens and adhesins and localize in the membrane surrounding the terminal organelle a single particle approach was taken. In order to finally demonstrate that, affinity purified P110 and P140 from *M. genitalium* were subjected to room temperature TEM to perform single particle reconstructions. Interestingly, processing of the projection obtained resulted in a very similar result when compared with the subtomogram averaging result after filtering the results to a similar resolution (Fig.4.26), supporting the view that P140 and P110 are the only components of the nap complex.

Given the fact that no nap-like particles are also observed in the grid it is possible that there are other conformation of the adhesins. However, this hypothesis not seem to be the real biological situation for many reasons. First, the particles not selected for averaging seem aberrant forms caused either by aggregation or the detergent. Second, ghosts' membranes revealed that the tetramer is the most frequent—and only—particle that can be visualized in the reconstructed volumes (Fig.4.5C). Third, a unique and homogeneous peak is observed by SEC prior to deposition of the particles over the grid.

The higher resolution achieved by single particle negative staining TEM revealed interesting features that allow to generate simplistic models about the mechanisms of P110 and P140 adhesins. It is possible that the 1.5 nm diameter groove in the upper part of the complex containing a 0.6 nm hole diagonally crossing the nap complex plays an important role in the motility mechanism. It has been described that sialylated compounds are capable to detach mycoplasma cells from gliding surfaces. Specifically, the known compound with the highest affinity for *M. pneumoniae* cells is Neu5Ac--2,3-lactosamine which is around 2.1 in length x 0.6 nm in width (assuming a linear form). Interestingly, such compound can perfectly fit in both the groove and the hole present in the surface of the top view of the complex. In a hypothetical scenario, the grove region of the complex present high affinity for sialylated compounds catching them with strength enough to promote movement once a force pull the particle against the movement direction. There is no evidence that the nap complex itself can generate that force, but it is possible that conformational changes will promote the travelling of the sialylated compound through the groove, creating a force capable of change of the position of the particle (Fig. 4.27).

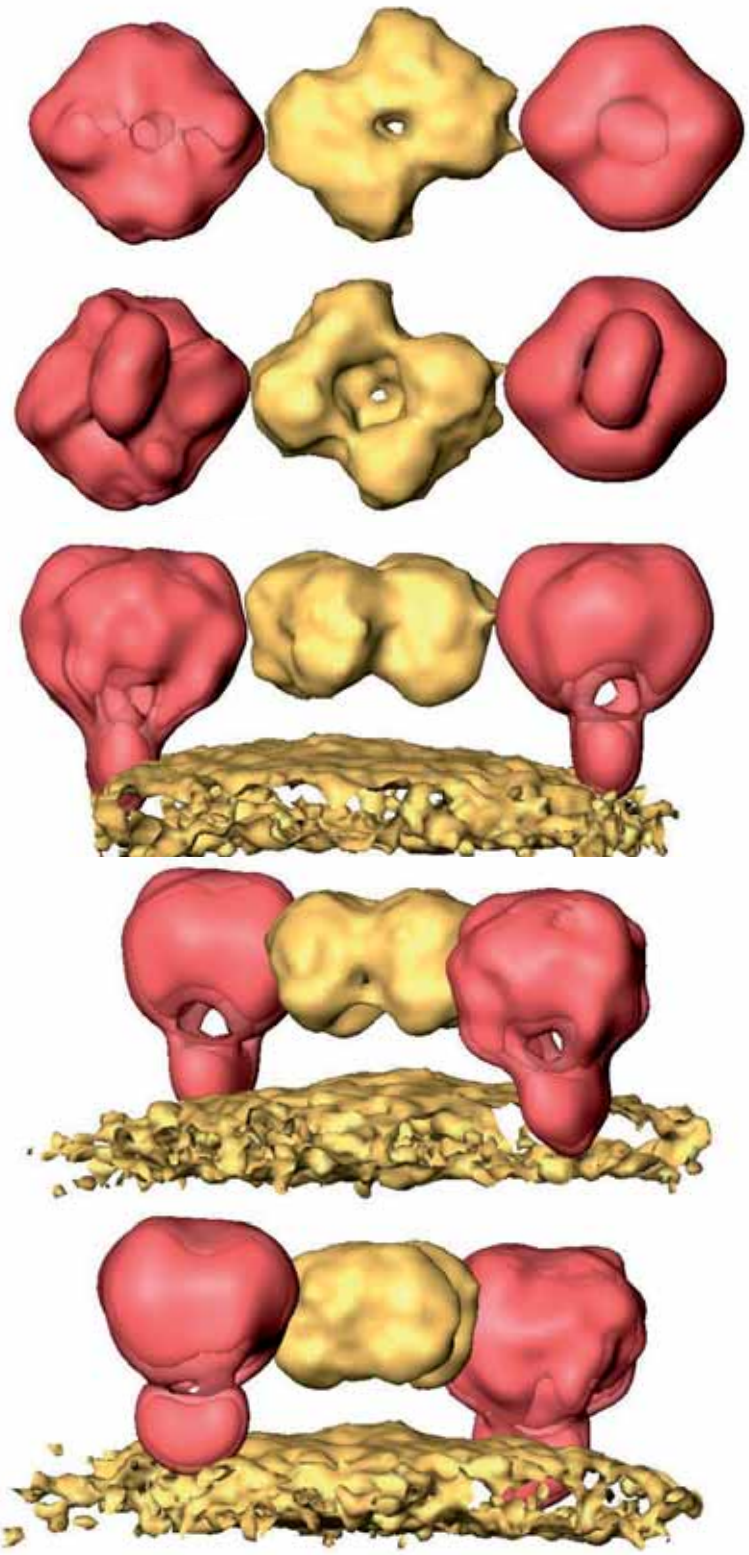

Figure 4.26. Comparison between the nap complex and P110 and P140 structures. Different views from the isosurfaces generated from the subtomogran averaging (yellow) and the single particle reconstruction (red). Two red structures are presented; in A, B and C de right red particle is the result of the averaging filtered to 3.5 nm resolution. In D and E the left particle is the simple particle averaging filtered to 3.5 nm resolution. The remaining red particles are the averaging result without filtering (1.9 nm resolution).

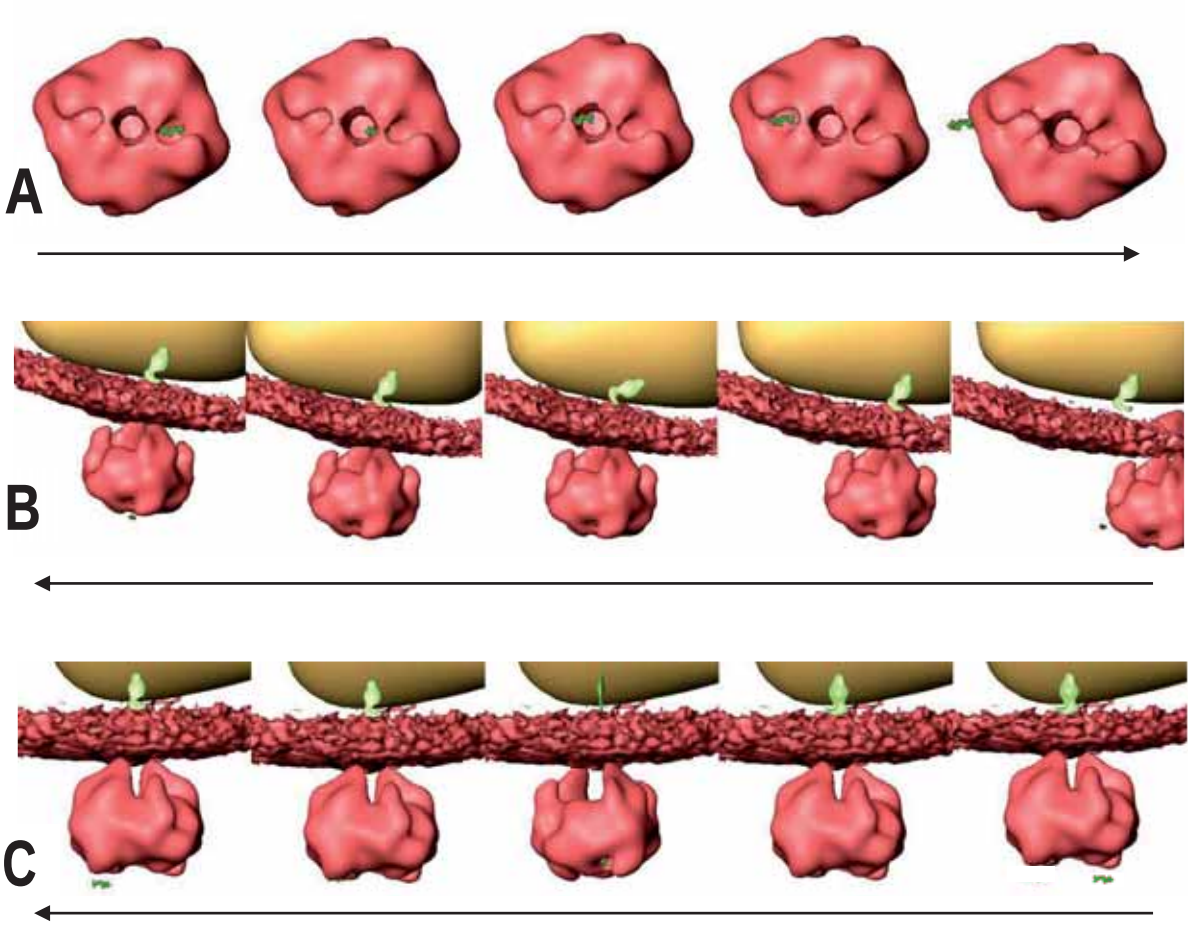

Figure 4.27. Model of how P110 and P140 nap complexes promote the movement over sialylated compound surfaces. Green and red minute spheres correspond a single molecule of a sialylated compound anchored to the surface. Arrows indicate the movement of the particle—and the cell. All sequences are time ordered from left to right. **A.** Sialylated compounds travel through the surface groove of the top of the particle, promoting the movement of the particle in the direction of the arrow. A major conformational change is needed to release the sialylated compound and its linker to the surface (which is not shown for clarity purposes). **B.** Leg model for P110 and P140 mechanism. P110 and P140 attach to sialylated compounds of the surface, then a force incoming from the cytoskeleton promotes the movement of the complex. Given the high quantity of the naps over the surface of *M. genitalium* terminal organelle, other complexes perform the same process, resulting in the detachment of the particle from the original sialylated compound, leaving the particle free to repeat the process. For clarity purposes other nap complexes and the linker of the sialylated compound to the cell membrane are not shown. **C.** Rotatory model for P110 and P140 complex. Once the complex gets attached to a sialylated compound a cytoskeleton structure promotes the rotation of the P110 and P140 protein. For clarity purposes other nap complexes and the linker of the sialylated compound to the cell membrane are not shown.

Another possibility is that the P110 and P140 complex acts as a 'leg' protein (Fig. 4.27B). In that theoretical situation, the nap will attach to one or more molecules of a sialylated compound over the gliding surface, and a relative strong force originating from the cytoskeleton will pull the nap in the opposite direction of the cell movement direction. The release of the sialylated compound can be regulated by a conformational change or can be consequence of the movement of other nap complexes moving in an uncoordinated fashion. Once the sialylated compound is released the process can be repeated indefinitely causing the movement of the cell.

The last possible scenario presented (Fig. 4.27C) is that the nap complex presents a rotational movement. For that purpose the cytoskeleton should promote the rotation of the nap complex from within the cell and the P110 and P140 complex should catch and release the sialylated compound each 180 degrees.

Although the existence of these hypotheses, the molecular mechanisms of how these complexes interact with the sialylated compounds of the media, extracellular matrix or cell surfaces, allowing the serial attachment and detachment to promote gliding motility is still a puzzling question. Using the latest developments in Cryo-EM and obtaining the high resolution averages from P110 and P140 particles—either from the cells, ghosts or isolated particles—may help answer this question.

Cryo-EM and CET have been proven useful not only for the analysis of the surface and internal macromolecular complexes of *M. genitalium* but also of its cell morphology and cellular processes (Fig. 4.28). Cell division seems to be preceded by the semiconservative division of the cytoskeleton, starting from the terminal button (Fig. 4.28A). Later on the terminal organelles start to depart from each other will they are at opposing poles (Fig. 4.28B, 4.28C and 4.28D). Then one or the two terminal organelles start to pull the cells in contrary directions, eventually forming two individual cells. This cell division model is completely equivalent to the one proposed for cell division in *M. pneumoniae*.

CET has also been proven useful for analysing the cytoskeleton and morphology mutant strains of terminal organelle proteins of *M. genitalium*. Mutants lacking MG_191 or MG192 gene showed exactly the same morphology and characteristics when CET analysed. This result is not surprising since both proteins are reciprocally stabilized. As expected, no nap complex is present in the membrane of any of the cells observed. Interestingly, most of the cells analysed presented multiple terminal organelle cytoskeletons. This could be consequence of as specific role of P110 and P140 in terminal organelle duplication or just a consequence of an impaired cell division. Since cells lacking P110 and P140 cannot attach to surfaces thus are not capable to perform gliding motility. In this condition cells would increase in biomass but not in number of cells, resulting in bigger cells with multiple terminal organelles. This situation also would explain the appearance of small cells without terminal organelle.

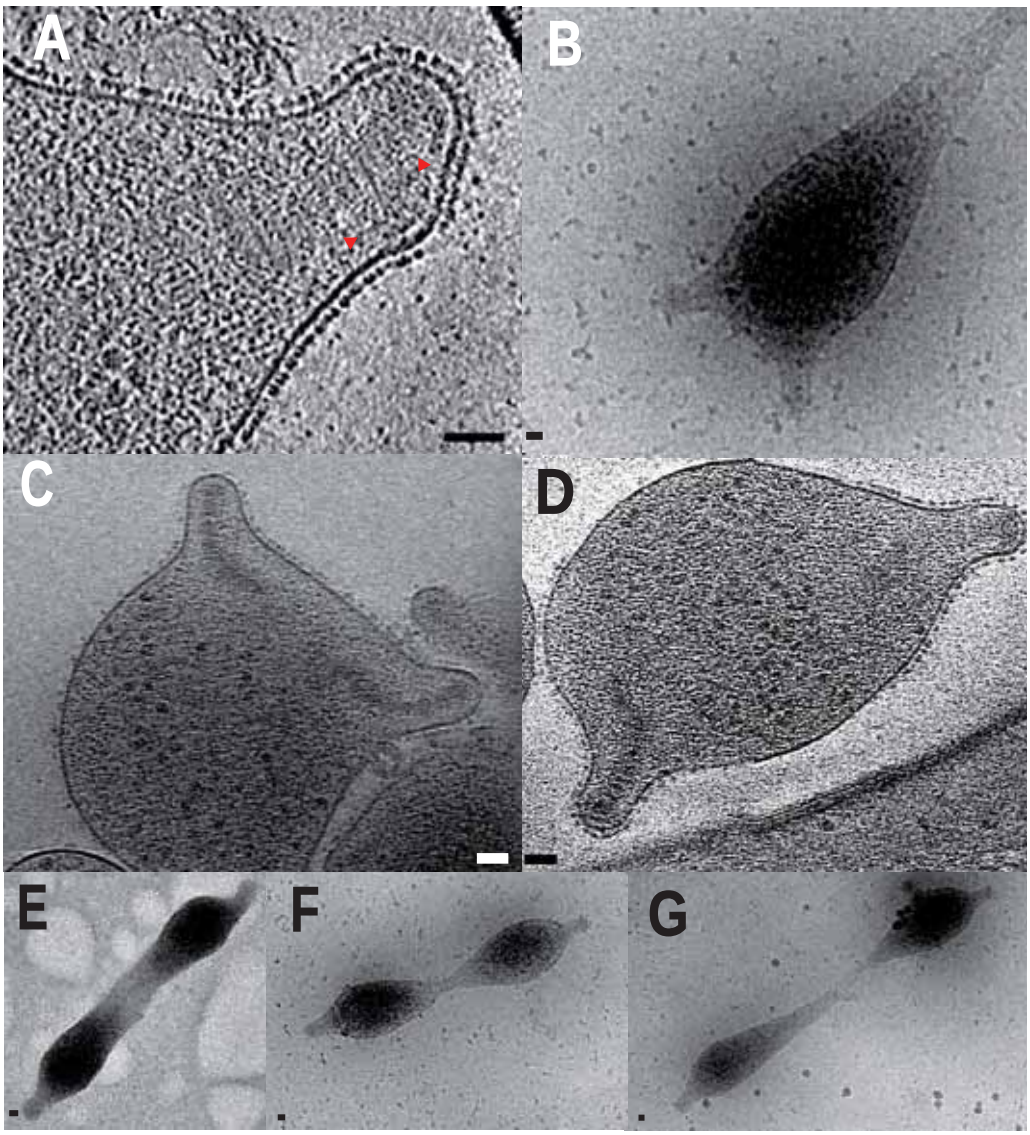

Figure 4.28. Cell division of *M. genitalium*. **A.** Average projection of fifteen 0.85 nm thick slices through the reconstructed volume of a top view of an early stage terminal organelle division. Red arrows delimitate a nascent terminal button almost 90º of the segmented paired plats. **B**. Cryo-EM image of two cytoskeletons ending its division and separating from each other. **C.** Average projection of fifteen 0.67 nm thick slices through the reconstructed volume of the side view of two independent cytoskeletons that have just completed its replication. **D.** Average projection of fifteen 0.67 nm thick slices through the reconstructed volume of the side view of two independent cytoskeletons in the opposite poles of the cell. **E, F & G.** Different stages of two terminal organelles pulling in opposite directions in the process of finishing gliding motility-assisted cell division. All cells are from the wild type strain except C (MG217 null mutant strain). Scale bars are 50 nm.

Strains presenting lack of MG218 and MG312 showed bigger pleomorphic cells and did not present any kind of cytoskeleton similar to the observables in the WT strain. This fact that this train does not present rod is not surprising since those to proteins and its orthologues in *M. pneumoniae* are thought to be the main components of the segmented paired plates. However, this strains still present wild-type levels of MG219, MG491, MG200, P32 and

reduced levels of MG317 so one will expect to see some terminal buttons or electron dense foci around the cell. Although it cannot be discarded that those cells present such structures, they have not been observed in the CET studies performed in this work.

MG217 and MG318 null mutant strains showed a decrease of a 15% in the size of the terminal button. Since ΔMG318 does not present MG217 protein in steady state levels, the most reasonable explanation for that decrease is—at least in part—consequence of the absence of MG217. Although no other important changes in the cytoskeleton or the morphology of the cells of ΔMG217 strain can be observed, ΔMG318 cells presented a high frequency of cytoskeletons not properly aligned relative to the cell membrane. Since P32 presents a N-terminal transmembrane domain it is possible that ΔMG318 cells do fail to anchor the terminal organelle to the membrane. Importantly, the cytoskeleton is always in association with the membrane surrounded by nap complexes, suggesting other factors playing a role in the co-localization of the cytoskeleton and the nap complexes. Unluckily, no cells with a thickened terminal organelle have been observed by CET. It is possible that given the relative low frequency of such terminal organelle they were not observed only by chance. More cells of ΔMG318 and ΔMG318C-ter strain should be analyses in the future to corroborate that. ΔMG318 and ΔMG318C-ter showed the exact same morphology by CET. The P110 and P140 levels are difficultly quantified by CET so it is not possible to discern if the strain lacking the whole gene present more naps than the strain retaining the N-terminal domain of P32.

All of ΔMG317 cells analysed presented an aberrant cytoskeleton—an electrondensity not reasonably resembling to anything previously seen in the WT strain. Importantly, there all of those aberrant cytoskeletons are still linked to nap surrounded membranes, reinforcing the view that there are other components playing a role in the of the nap complex association with the cytoskeleton. The reason why filaments connecting two different cells are recovered by nap complexes is still puzzling. However, since some of the ΔMG317 cells in are capable to glide at reasonable speeds (40% of the WT) it is possible that a cytoskeleton similar to the WT is present in some cells, however, they have been not observed.

Cells lacking MG491 or MG386 showed a very similar phenotype; long filaments protruding from cells with a cytoskeleton lacking the wheel-like complex. These strains also present an important number of minute cells or terminal organelle-only cells, most likely caused by the detachment of the cytoskeleton containing particles in the tip of the filaments. Interestingly those detached cytoskeletons are completely covered by nap particles, indicating that cytoskeletons are capable of moving themselves without the cell body during an unkwon period of time. One might think that these structures—terminal button plus the segmented

paired plates—are the minimal motile machinery for generating gliding motility, but recent results are against that view[11]. Mutants lacking the central and C-ter region of MG386 showed terminal organelles containing cytoskeletons with a distinctive curvature, suggesting an important role of MG386 in the flexibility of the cytoskeleton. No other important effects were observed, suggesting that N-ter of MG386 is mandatory for anchoring the terminal organelle to the cell body, but not for the stability of the cytoskeleton itself. The main difference of the phenotype of M386 and MG491 null mutants is that MG491 have been shown to be essential for the stability of all the known proteins of the terminal organelle except from those which localizes at the wheel-complex.

Although the C-terminal of MG200 protein seems not critical for the formation of wild-type cytoskeleton structures, many of the cells analysed presented non-properly formed, suggesting a role in protein folding or terminal organelle formation. This is in agreement with the high number of multiple TO cells present in this strain. It is possible that low number of cells capable to perform gliding motility is due to the inability to form WT TOs at the standard ratio.

MG219 and MG218-s null mutants revealed no major affectations in the terminal organelle ultrastructure. Considering the low molecular weight of these proteins this result is not surprising, but given the phenotype of those strains, is it possible that this proteins are tiny structural pieces of the cytoskeleton essential for its proper functioning.

[11] In next section (general discussion) it will be shown that segmented paired plates are not required for gliding motility.

8. General discussion

Up to the present time, the knowledge of the cytoskeleton of *M. genitalium* was limited and most of the information was inferred by comparison with data obtained from *M. pneumoniae*. In this work we present the first data with enough detail to observe the substructures of the macromolecular complexes constituting the terminal organelle. In addition, we have shown that MG219, MG318 and MG386 have an important role in gliding motility or are important parts of the cytoskeleton. A proposed model of protein localization within the terminal organelle of all the known components is presented in Fig. D.1. In table D.1, a summary of all the effects observed to date in mutants with major deficiencies in one or more proteins of the terminal organelle is presented.

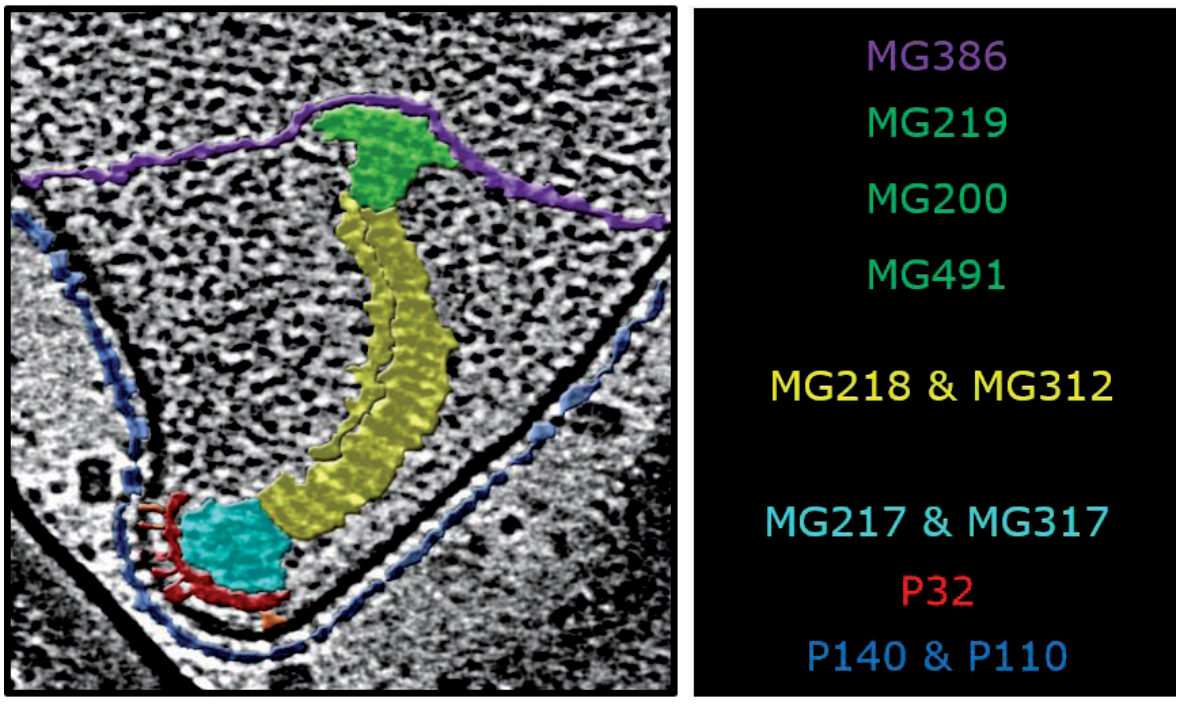

Figure D.1. Localization model for terminal organelle related proteins within the cytoskeleton of *M. genitalium*.

Given the fact that in all mutant strains that still have cytoskeleton present the nap in the membrane surrounding the cytoskeleton, it is possible that there is a protein product linking the nap to the cytoskeleton in the electronlucent area, MG218, MG312 or other unknown protein could be responsible for that (hypothesis not shown in Fig. D.1).

Table D.1.Summary of cell morphology and gliding motility characteristics of *M. genitalium* mutant strains lacking major parts of the coding gene for terminal organelle proteins.

				Motility						
Loci	**Protein**	**Mutant strain**	**Adhesion[#]**	**Frequency***	**Speed**	**Circular**	**Erratic**	**Track Ø**	**Cytoskeleton[&]**	**Cell morphology[+]**
-	-	WT	+++	100%	100%	84%	16%	100%	+++	+++
mg191	P140	ΔP140	-	0%	0%	NA	NA	NA	+++	+
mg192	P110	ΔP110	-	0%	0%	NA	NA	NA	+++	+
mg200	MG200	mg200^{-}	+++	5%	10%	5%	95%	NA	++	++
mg217	MG217	ΔMG_217	+++	97%	100%	37%	63%	141%	++	+++
mg218	MG218	ΔMG218	+	0%	NA	NA	NA	NA	-	+
c-ter mg218	MG218-s	MD-P3	+++	100%	116%	74%	26%	165%	+++	+++
mg219	MG219	Δmg219	+++	39%	40%	75%	25%	110%	+++	++
mg312	MG312	ΔMG_312	-	0%	0%	84%	16%	NA	-	+
mg317	MG317	Δmg317	+	4%	40%	5%	95%	120%	+	+
mg318	P32	Δmg318	++	43%	29%	84%	16%	158%	++	++
mg386	MG386	Δmg386	++	43%	170%	99%	1%	65%	++	+
mg386	MG386	mg386 GD c5	++	20%	35%	77%	23%	95%	+++	+++
mg491	MG491	ΔMG491	+	<0.1%	<0.1%	NA	NA	NA	++	+

[#]Adhesion: +++ WT, ++ >50%, + <50%, - <10%. The adhesion was qualitatively assessed on plastic when all strains were grown for CET.
[&]Cytoskeleton: +++ WT, ++ minor changes such as smaller parts or high frequency of division TOs, + pleomorphic cytoskeletons, - no cytoskeleton is observed
[+]Cell morphology: +++ WT, ++ high frequency of cells in division, + major changes such as minute cells, bigger cells or not flask-shaped cells.
* All values were adjusted to the gliding frequency of the WT strain in (Burgos et al., 2008). The reported gliding frequency in that article is 88.9%.

Path defining factors of gliding motility

Two proteins seems to have an important role in the definition of erratic or circular movements by *M.genitalium* cells: MG217 and MG386. While MG217 seems critical to maintain most of the cells depicting circular tracks, MG386 showed to have the opposite role. It is interesting to found that two proteins localizing in the most distant parts of the cytoskeleton (the terminal button and the wheel complex) are responsible for the erratic or circular movements. It is possible that MG217 actively promotes the circular movement, and MG386 actively prevents that the circular movement is not extremely narrow by straightening the terminal organelle with the cell body, when those proteins are in the wild-type ratio the equilibrium is broken causing higher frequencies of erratic or circular movements. It is possible that the crucial role of MG386 anchoring the terminal organelle to the cell body is the responsible for preventing the excessive curvature of the terminal organelle that would cause a higher frequency of circular tracks.

Determinant factors for the diameter of circular tracks depicted by gliding motility

In agreement with the path defining factors of gliding motility MG386 and MG217 are also involved in the diameter of depicted circular tracks. A direct correlation of erratic paths with larger diameter of the circular tracks and vice versa is observed. Interestingly, another protein located in the terminal button—MG318—present wider circular tracks. MG218-s, a protein of unknown location but most likely forming part of the segmented paired plates have been found to be also important for the diameter of circular tracks. Apparently, there is no correlation with this events, suggesting a coordinated mechanism of this proteins to obtaining the WT diameter circular track.

Gliding speed and frequency determinants

Remarkably, all of the strains with defects in gliding velocity also present defects in gliding speed (Table D.1). The most critical proteins for gliding speed have been shown to be MG491 and MG200, both proteins of the wheel-like complex. It is noteworthy the fact that after the addition of an extra copy of P32 to ΔMG491 strain the gliding speed half of the WT, discarding a major role of MG491 in the generation in the terminal organelle movement. Cells of mg200$^-$ in contrast, are able to glide at notably reduced speeds and frequencies, but given its co-chaperone putative role, the most reasonable explanation is that the terminal organelles or the adhesion complexes present important folding problems thus extremely limiting the gliding capabilities of this strain. Moreover, mild reductions of the gliding speed and frequency of the cells of in Δmg219, Δmg318 can be observed. Similar intermediate gliding

phenotypes can be observed in strains carrying mutations in domains of MG386, MG200 and MG312 (Pich et al., 2006, Martinelli et al., 2015, Calisto et al., 2012, Burgos et al., 2007). Interestingly, Δmg386 is the sole which cells are capable to glide at remarkable higher speeds than the WT strain. There is not a single mutant with affectations in the gliding speed able to glide at WT frequencies. All this data taken together suggest that the gliding apparatus is even more complex than previously envisioned. The interplay of proteins involved in gliding motility and the key protein (or proteins) needed for force generation is still need to be determined.

Structures of macromolecular complexes of the terminal organelle

The low-resolution terminal button structure revealed also the structure of the closer segmented paired plates relative to the terminal button. Interestingly, those plates seems to be in fact rings of 20 nm of diameter. A systematic study by recombinant expression of the terminal organelle proteins in *E. coli* is being performed in collaboration with Ignacio Fita (IBMB) and Barbara Calisto (ESRF/IBMC). Interestingly, one the proteins capable to be produced and purified in relative high amounts MG312—which is thought to be one of the main components of the segmented paired plates—present a structure of a 20 nm ring when observed by negative staining TEM (Fig. D.2). This data is in agreement with the hypothesis that MG312 is one of the major components of the segmented paired plates. Unluckily, the purification of MG218—the other possible major component of the segmented paired plates—have not been achieved and further conclusions cannot be taken.

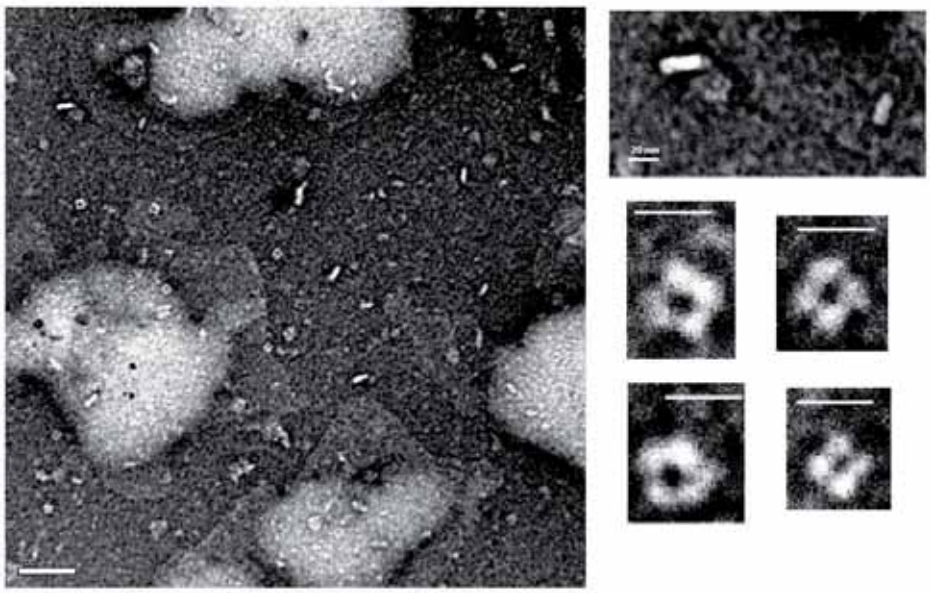

Figure D.2. Negative staining electron micrograph of the P110 and p140 purified from *E.coli* at different magnifications. Scale bar over the single particles is 20 nm. Images kindly provided by Mercè Ratera.

Since a mutant lacking the whole MG200 coding region also loses the expression of P140 and P110 but maintains wild-type levels of all the other proteins related with the terminal organelle, it is expected that the morphology of the cells are identical to mg191⁻ and mg192⁻ strains, but it is still needed to be determined.

In addition, null mutant for MG386 would be an excellent platform—given the relative high frequency of detached terminal organelles—to structurally characterize by CET the composition of the terminal button and the segmented paired plates. An alternative for doing so, would be the study of the whole terminal organelle by CET from ghosts cells, taking extreme caution of the artefacts that Triton X-100 treatment can do to the cells.

It is also very interesting the finding that a lamellar septum separating the cytoskeleton area from the cytoplasm has been detected for first time. It is feasible to hypothesize that this septum is composed by MG386 or MG491 protein. Supporting this view, P110 and P140 null mutants present WT levels of all proteins except of MG386, and CET analysis of its cells revealed that all the components of the cytoskeleton are present except from the lamellar septum. In addition, the point of contact of the lamellar structure with the cell membrane is always close to the end of the nap-covered membrane, suggesting a direct interaction of the nap complex with the septum. Moreover, strains lacking that septum will lose the connection to the cell membrane and the cell body, which is exactly the phenotype observed in ΔMG386 strain—the detached terminal organelles. All these facts reinforce the hypothesis that the main component of the lamellar septum is MG386.

A terminal organelle driven model for gliding motility?

Recently, it has been shown that a strain lacking MG218 but harbouring an extra copy of MG318:mCherry in the genome is capable to glide near at half of the speed of the wild-type strain (Garcia, L. manuscript in preparation). Interestingly, when those cells were analysed by cryo-EM mostly all cells presented a circular of spherical electrondense core surrounded by nap structures at the tip of the filaments or the cells of this strain (Fig. D3).

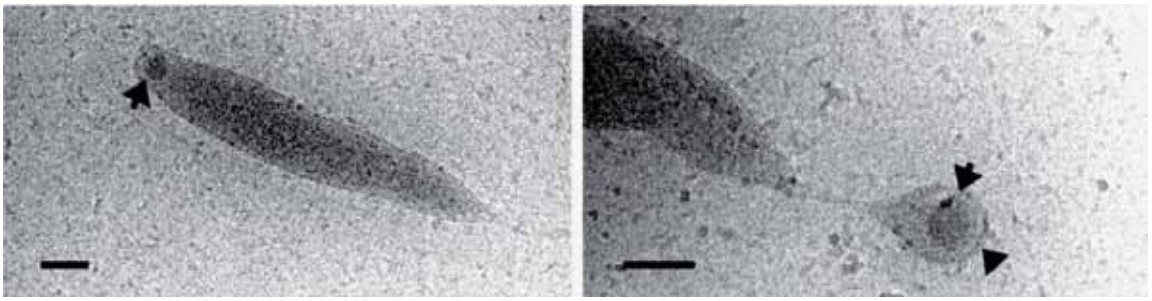

Figure D.3. Ultrastructure of cells and filaments from M. genitalium Δmg218-P32ch mutant strain by cryo-EM. Filaments and cells from Δmg218-P32ch strain showing circular electron dense cores in one of their ends (black arrows). Black triangle point to the nap structures that were only detected in the membrane surrounding the electron dense cores. Scale bars are 300 nm.

Those results in combination with the microcinematographies showing that this cells are capable to glide suggest that the cytoskeleton—at least the WT cytoskeleton—is not essential for movement generation and gliding motility.

The composition of this spherical or circular electrondense core is unknown. Since WT levels of MG491, MG200, MG219 and reduced amounts of MG386 and MG317 are present in this strain, one can hypothesize that it is composed by at least a combination of these proteins, if not more unknown components of the cytoskeleton .

The wheel-like complex have been also found not to be critical for gliding motility, since cells lacking it (ΔMG386 and ΔMG491) are capable to glide.

With this scenario, one would think that the terminal button is the responsible of generation of the gliding motility of *M. genitalium*. But three main components are known of the terminal button: P32, MG217 and MG317, and strains lacking any of those proteins are capable to glide at WT or near 40% of the wild-type speed.

Noteworthy is the fact that none of the strains lacking any of those proteins are completely not motile—except from the ones without nap, which are incapable to attach to surfaces in normal conditions.

Taken all this data together one can conclude that either P110-P140 complex is the responsible itself for the generation of the movement or there is an unidentified protein performing that function. Since no ATPase, GTPase, proton pump or similar domains are detected by sequence analysis of the sequence of the proteins of the terminal organelle further experiments are needed to found the energy source of the gliding motility, which could lead to the identification of the key element that generates the movement of the cytoskeleton and the cells. Another possible explanation is that the cytoskeleton of *M. genitalium* contains more than one component capable to use energy sources to perform gliding motility. Given the low sequence similarity (except from the EAGR boxes)

In that way, one can propose a model for gliding motility with all the information gathered. Each part of the cytoskeleton would perform a specific role in the gliding motility process. The different parts of the cytoskeleton one would be critical for different steps in gliding motility. The first step would be catching the sialylated compound on the surface. Given that the terminal button is the most exposed part of the terminal organelle when a cell is moving forward, it is likely that the naps surrounding the terminal button are the responsible of the initial attachment to the surface. Later, a conformational change—either incoming from the terminal button through, for example, P32 or directly promoted by the nap complex itself—would cause the nap complex to move in an unknown fashion, causing a displacement of the nap relative to the surface. This process would occur dozens or hundreds of times most likely coordinated by the terminal button. Since the nap is in close connection with the cytoskeleton, this movement would be inmmediatly transmitted to the segmented paired plates and the wheel-like complex, moving the cytoskeleton—but not the cell—towards the direction of the movement. In that situation, the lamellar septum at the end of the cytoskeleton—most likely formed by MG386—would be suffering an important tension. The components of the wheel complex (MG491, MG200, MG219 and MG386) will actively release that tension to the cell body, causing a movement. It is likely that hundreds of nap 'unitary steps' are needed for generating the tension enough, that once released, will cause the whole cell body to move.

9. Conclusions

- MG219 protein is a key protein for gliding motility. Cells of a strain lacking this small polypeptide glide 60% less frequently and at gliding speeds 60% lower than the WT strain. In agreement with that finding, cells with multiple terminal organelle or in process or cell division are abundant in this strain.
- Orthologous gene replacement of MG219 protein for P24 protein of *M. pneumoniae* generated a strain presenting and intermediate phenotype between MG219 and P24. This results suggest that MG219 and MPN312 genes have a common ancestor but rapidly evolved to be different proteins with similar but no the exact same function.

- P32 protein, in contrast that what have been found in *M.* pneumoniae, is not essential for gliding motility or adhesion. Although a moderate impact in gliding speed and frequency is observed (43% of gliding frequency and 29% of gliding speed), the most common cell morphology observed is the characteristic flask shape of the WT strain. Cells lacking P32 also depict wider circular tracks than the reference strain.
- P32 protein have been shown to be critical for maintaining WT levels of P110 and P140 adhesins. Interestingly, a strain lacking only the C-terminal presented near-WT levels of the main adhesins, suggesting a specific role of the N-ter of P32 in the stabilization of P110 and P140.
- The lack of P32 protein affects terminal organelle morphology. Mostly all cells of strains lacking either P32 or P32C-ter present a smaller terminal button. Cells that did not present that small terminal button present a thickened terminal organelle.
- CET of P32 mutant strains confirmed the smaller terminal button and also revealed that most of the cells are incapable of properly align the cytoskeleton to the cell membrane surrounding the terminal organelle.

- MG386 have been shown to be critical for maintaining cell morphology and gliding frequency. Almost no flask-shaped cells can be observed in strains lacking MG386 but a high frequency of terminal organelle detachments and filaments protruding from cell bodies are detected.

- The gliding speed of the detached cells are 70% of the wild type strain, but normal sized cells glide at a mean speed 70% higher than the wild-type, suggesting that MG386 is also a negative effector of gliding speed.
- Almost all cells of strains lacking MG386 glide depicting circular tracks that also are 35% narrower than those depicted by the wild-type train.

- Determining the structure of the nap complex at 3.5 nm by CET and the structure of P110 and P140 by negative staining TEM at 1.9 nm showed that the nap is formed only by a tetramer of P110 and P140, most likely in a dimer of heterodimers fashion.
- CET has proven useful for the analysis of the cytoskeleton of *M. genitalium*. The analyses revealed a structure very similar to the one described to *M. pneumoniae* (terminal button, segmented paired plates and a wheel-like complex) in addition to a 4 nm thick lamellar structure at the end of the wheel-like complex.
- Low resolution averaging of the terminal button from ghost cells revealed that the segmented paired plates are in fact formed by 20 nm diameter rings, most likely formed by MG312 and maybe also MG218.
- CET of mutants lacking all the known proteins of the terminal organelle showed that:
    - P110 and P140 mutants present no nap on the surface but WT cytoskeletons can be observed inside the cell
    - MG318 and MG217 are two of the main components of the terminal button
    - MG317 is critical for maintaining the proper cytoskeleton morphology
    - Cells lacking either MG218 or MG312 do not present any form of cytoskeleton
    - MG386 and MG491 are critical for the wheel-like complex formation and also for anchoring the segmented paired plates plus the terminal button and the nap to the cell body
    - MG200 protein is not critical for the structure of any of the components of the cytoskeleton, but cells lacking the C-ter of this protein usually present abnormal cytoskeletons, suggesting a role of this protein in protein folding or terminal organelle
    - Cells lacking MG219 or MG218-s does not present detectable alterations of the cytoskeleton